

JUNO sensitivity to ${}^7\text{Be}$, *pep*, and CNO solar neutrinos

Angel Abusleme^{6,5} Thomas Adam⁴⁵ Shakeel Ahmad⁶⁶ Rizwan Ahmed⁶⁶ Sebastiano Aiello⁵⁵ Muhammad Akram⁶⁶ Abid Aleem⁶⁶ Tsagkarakis Alexandros⁴⁸ Fengpeng An²¹ Qi An²³ Giuseppe Andronico⁵⁵ Nikolay Anfimov⁶⁷ Vito Antonelli⁵⁷ Tatiana Antoshkina⁶⁷ Burin Asavapibhop⁷¹ João Pedro Athayde Marcondes de André⁴⁵ Didier Auguste⁴³ Weidong Bai²¹ Nikita Balashov⁶⁷ Wander Baldini⁵⁶ Andrea Barresi⁵⁸ Davide Basilico⁵⁷ Eric Baussan⁴⁵ Marco Bellato⁶⁰ Marco Beretta⁵⁷ Antonio Bergnoli⁶⁰ Daniel Bick⁴⁹ Lukas Bieger⁵⁴ Svetlana Biktemerova⁶⁷ Thilo Birkenfeld⁴⁸ David Blum⁵⁴ Simon Blyth¹¹ Anastasia Bolshakova⁶⁷ Mathieu Bongrand⁴⁷ Clément Bordereau^{44,40} Dominique Breton⁴³ Augusto Brigatti⁵⁷ Riccardo Brugnera⁶¹ Riccardo Bruno⁵⁵ Antonio Budano⁶⁴ Jose Bustos⁴⁶ Anatael Cabrera⁴³ Barbara Caccianiga⁵⁷ Hao Cai³⁴ Xiao Cai¹¹ Yanke Cai¹¹ Zhiyan Cai¹¹ Stéphane Callier⁴⁴ Antonio Cammi⁵⁹ Agustin Campeny^{6,5} Chuanya Cao¹¹ Guofu Cao¹¹ Jun Cao¹¹ Rossella Caruso⁵⁵ Cédric Cerna⁴⁴ Vanessa Cerrone^{61,60} Chi Chan³⁸ Jinfan Chang¹¹ Yun Chang³⁹ Chao Chen¹¹ Guoming Chen²⁸ Pingping Chen¹⁹ Shaomin Chen¹⁴ Yixue Chen¹² Yu Chen²¹ Zhiyuan Chen¹¹ Zikang Chen²¹ Jie Cheng¹² Yaping Cheng⁸ Yu Chin Cheng⁴⁰ Alexander Chepurnov⁶⁹ Alexey Chetverikov⁶⁷ Davide Chiesa⁵⁸ Pietro Chimenti³ Ziliang Chu¹¹ Artem Chukanov⁶⁷ Gérard Claverie⁴⁴ Catia Clementi⁶² Barbara Clerbaux² Marta Colomer Molla² Selma Conforti Di Lorenzo⁴⁴ Alberto Coppi^{61,60} Daniele Corti⁶⁰ Simon Csakli⁵² Flavio Dal Corso⁶⁰ Olivia Dalager⁷⁴ Jaydeep Datta² Christophe De La Taille⁴⁴ Zhi Deng¹⁴ Ziyan Deng¹¹ Wilfried Depnerring⁵¹ Xiaoyu Ding²⁶ Xuefeng Ding¹¹ Yayun Ding¹¹ Bayu Dirgantara⁷³ Carsten Dittrich⁵² Sergey Dmitrievsky⁶⁷ Tadeas Dohnal⁴¹ Dmitry Dolzhikov⁶⁷ Georgy Donchenko⁶⁹ Jianmeng Dong¹⁴ Evgeny Doroshkevich⁶⁸ Wei Dou¹⁴ Marcos Dracos⁴⁵ Frédéric Druillole⁴⁴ Ran Du¹¹

Shuxian Du³⁷ Katherine Dugas⁷⁴ Stefano Dusini⁶⁰ Hongyue
Duyang²⁶ Jessica Eck⁵⁴ Timo Enqvist⁴² Andrea Fabbri⁶⁴ Ulrike
Fahrendholz⁵² Lei Fan¹¹ Jian Fang¹¹ Wenxing Fang¹¹ Marco
Fargetta⁵⁵ Dmitry Fedoseev⁶⁷ Zhengyong Fei¹¹ Li-Cheng Feng³⁸
Qichun Feng²² Federico Ferraro⁵⁷ Amélie Fournier⁴⁴ Haonan
Gan³² Feng Gao⁴⁸ Alberto Garfagnini⁶¹ Arsenii Gavrikov^{61,60}
Marco Giammarchi⁵⁷ Nunzio Giudice⁵⁵ Maxim Gonchar⁶⁷
Guanghua Gong¹⁴ Hui Gong¹⁴ Yuri Gornushkin⁶⁷ Alexandre
Göttel^{50,48} Marco Grassi⁶¹ Maxim Gromov⁶⁹ Vasily Gromov⁶⁷
Minghao Gu¹¹ Xiaofei Gu³⁷ Yu Gu²⁰ Mengyun Guan¹¹ Yuduo
Guan¹¹ Nunzio Guardone⁵⁵ Cong Guo¹¹ Wanlei Guo¹¹ Xinheng
Guo⁹ Caren Hagner⁴⁹ Ran Han⁸ Yang Han²¹ Miao He¹¹ Wei
He¹¹ Tobias Heinz⁵⁴ Patrick Hellmuth⁴⁴ Yuekun Heng¹¹ Rafael
Herrera^{6,5} YuenKeung Hor²¹ Shaojing Hou¹¹ Yee Hsiung⁴⁰
Bei-Zhen Hu⁴⁰ Hang Hu²¹ Jianrun Hu¹¹ Jun Hu¹¹ Shouyang
Hu¹⁰ Tao Hu¹¹ Yuxiang Hu¹¹ Zhuojun Hu²¹ Guihong Huang²⁵
Hanxiong Huang¹⁰ Jinhao Huang¹¹ Junting Huang³⁰ Kaixuan
Huang²¹ Wenhao Huang²⁶ Xin Huang¹¹ Xingtao Huang²⁶
Yongbo Huang²⁸ Jiaqi Hui³⁰ Lei Huo²² Wenju Huo²³ Cédric
Huss⁴⁴ Safeer Hussain⁶⁶ Leonard Imbert⁴⁷ Ara Ioannision¹
Roberto Isocrate⁶⁰ Beatrice Jelmini⁶¹ Ignacio Jeria⁶ Xiaolu Ji¹¹
Huihui Jia³³ Junji Jia³⁴ Siyu Jian¹⁰ Cailian Jiang²⁷ Di Jiang²³
Wei Jiang¹¹ Xiaoshan Jiang¹¹ Xiaoping Jing¹¹ Cécile Jollet⁴⁴
Philipp Kampmann^{53,50} Li Kang¹⁹ Rebin Karaparambil⁴⁷ Narine
Kazarian¹ Ali Khan⁶⁶ Amina Khatun⁷⁰ Khanchai
Khosonthongkee⁷³ Denis Korablev⁶⁷ Konstantin Kouzakov⁶⁹
Alexey Krasnoperov⁶⁷ Sergey Kuleshov⁵ Nikolay Kutovskiy⁶⁷
Tobias Lachenmaier⁵⁴ Cecilia Landini⁵⁷ Sébastien Leblanc⁴⁴
Victor Lebrin⁴⁷ Frederic Lefevre⁴⁷ Ruiting Lei¹⁹ Rupert Leitner⁴¹
Jason Leung³⁸ Demin Li³⁷ Fei Li¹¹ Fule Li¹⁴ Gaosong Li¹¹ Huiling
Li¹¹ Jiajun Li²¹ Mengzhao Li¹¹ Min Li¹¹ Nan Li¹⁷ Qingjiang Li¹⁷
Ruhui Li¹¹ Rui Li³⁰ Shanfeng Li¹⁹ Tao Li²¹ Teng Li²⁶ Weidong
Li^{11,15} Weiguo Li¹¹ Xiaomei Li¹⁰ Xiaonan Li¹¹ Xinglong Li¹⁰ Yi
Li¹⁹ Yichen Li¹¹ Yufeng Li¹¹ Zepeng Li¹¹ Zhaohan Li¹¹ Zhibing
Li²¹ Ziyuan Li²¹ Zonghai Li³⁴ Hao Liang¹⁰ Hao Liang²³ Jiajun
Liao²¹ Ayut Limphirat⁷³ Guey-Lin Lin³⁸ Shengxin Lin¹⁹ Tao Lin¹¹
Jajie Ling²¹ Xin Ling²⁴ Ivano Lippi⁶⁰ Caimei Liu¹¹ Fang Liu¹²
Fengcheng Liu¹² Haidong Liu³⁷ Haotian Liu³⁴ Hongbang Liu²⁸
Hongjuan Liu²⁴ Hongtao Liu²¹ Hui Liu²⁰ Jianglai Liu^{30,31} Jiaxi

Liu¹¹ Jinchang Liu¹¹ Min Liu²⁴ Qian Liu¹⁵ Qin Liu²³ Runxuan
Liu^{50,48} Shenghui Liu¹¹ Shubin Liu²³ Shulin Liu¹¹ Xiaowei Liu²¹
Xiwen Liu²⁸ Xuewei Liu¹⁴ Yankai Liu³⁵ Zhen Liu¹¹ Alexey
Lokhov^{69,68} Paolo Lombardi⁵⁷ Claudio Lombardo⁵⁵ Kai Loo⁵¹
Chuan Lu³² Haoqi Lu¹¹ Jingbin Lu¹⁶ Junguang Lu¹¹ Peizhi Lu²¹
Shuxiang Lu³⁷ Bayarto Lubsandorzhev⁶⁸ Sultim
Lubsandorzhev⁶⁸ Livia Ludhova^{50,48} Arslan Lukanov⁶⁸ Daibin
Luo¹¹ Fengjiao Luo²⁴ Guang Luo²¹ Jianyi Luo²¹ Shu Luo³⁶
Wuming Luo¹¹ Xiaojie Luo¹¹ Vladimir Lyashuk⁶⁸ Bangzheng
Ma²⁶ Bing Ma³⁷ Qiumei Ma¹¹ Si Ma¹¹ Xiaoyan Ma¹¹ Xubo Ma¹²
Jihane Maalmi⁴³ Marco Magoni⁵⁷ Jingyu Mai²¹ Yury
Malyshkin^{53,50} Roberto Carlos Mandujano⁷⁴ Fabio Mantovani⁵⁶
Xin Mao⁸ Yajun Mao¹³ Stefano M. Mari⁶⁴ Filippo Marini⁶¹
Agnese Martini⁶³ Matthias Mayer⁵² Davit Mayilyan¹ Ints
Mednieks⁶⁵ Yue Meng³⁰ Anita Meraviglia^{53,50,48} Anselmo
Meregaglia⁴⁴ Emanuela Meroni⁵⁷ David Meyhöfer⁴⁹ Lino
Miramonti⁵⁷ Nikhil Mohan^{53,50,48} Paolo Montini⁶⁴ Michele
Montuschi⁵⁶ Axel Müller⁵⁴ Massimiliano Nastasi⁵⁸ Dmitry V.
Naumov⁶⁷ Elena Naumova⁶⁷ Diana Navas-Nicolas⁴³ Igor
Nemchenok⁶⁷ Minh Thuan Nguyen Thi³⁸ Alexey Nikolaev⁶⁹
Feipeng Ning¹¹ Zhe Ning¹¹ Hiroshi Nunokawa⁴ Lothar
Oberauer⁵² Juan Pedro Ochoa-Ricoux^{74,6,5} Alexander
Olshevskiy⁶⁷ Domizia Orestano⁶⁴ Fausto Ortica⁶² Rainer
Othegraven⁵¹ Alessandro Paoloni⁶³ Sergio Parmeggiano⁵⁷ Yatian
Pei¹¹ Luca Pelicci^{50,48} Anguo Peng²⁴ Haiping Peng²³ Yu Peng¹¹
Zhaoyuan Peng¹¹ Frédéric Perrot⁴⁴ Pierre-Alexandre Petitjean²
Fabrizio Petrucci⁶⁴ Oliver Pilarczyk⁵¹ Luis Felipe Piñeres Rico⁴⁵
Artyom Popov⁶⁹ Pascal Poussot⁴⁵ Ezio Previtali⁵⁸ Fazhi Qi¹¹
Ming Qi²⁷ Xiaohui Qi¹¹ Sen Qian¹¹ Xiaohui Qian¹¹ Zhen Qian²¹
Hao Qiao¹³ Zhonghua Qin¹¹ Shoukang Qiu²⁴ Gioacchino
Ranucci⁵⁷ Reem Rasheed⁴⁴ Alessandra Re⁵⁷ Abdel Rebii⁴⁴ Mariia
Redchuk⁶⁰ Bin Ren¹⁹ Jie Ren¹⁰ Barbara Ricci⁵⁶ Mariam Rifai^{50,48}
Mathieu Roche⁴⁴ Narongkiat Rodphai¹¹ Aldo Romani⁶² Bedřich
Roskovec⁴¹ Xichao Ruan¹⁰ Arseniy Rybnikov⁶⁷ Andrey
Sadovsky⁶⁷ Paolo Saggese⁵⁷ Deshan Sandanayake⁴⁵ Simone
Sanfilippo⁶⁴ Anut Sangka⁷² Utane Sawangwit⁷² Michaela
Schever^{50,48} Cédric Schwab⁴⁵ Konstantin Schweizer⁵² Alexandr
Selyunin⁶⁷ Andrea Serafini⁶¹ Mariangela Settimo⁴⁷ Vladislav
Sharov⁶⁷ Arina Shaydurova⁶⁷ Jingyan Shi¹¹ Yanan Shi¹¹ Vitaly

Shutov⁶⁷ Andrey Sidorenkov⁶⁸ Fedor Šimkovic⁷⁰ Apeksha
Singhal^{50,48} Chiara Sirignano⁶¹ Jaruchit Siripak⁷³ Monica Sisti⁵⁸
Mikhail Smirnov²¹ Oleg Smirnov⁶⁷ Thiago Sogo-Bezerra⁴⁷
Sergey Sokolov⁶⁷ Julianan Songwadhana⁷³ Boonrucksar
Soonthornthum⁷² Albert Sotnikov⁶⁷ Ondřej Šrámek⁴¹ Warintorn
Sreethawong⁷³ Achim Stahl⁴⁸ Luca Stanco⁶⁰ Konstantin
Stankevich⁶⁹ Hans Steiger^{51,52} Jochen Steinmann⁴⁸ Tobias
Sterr⁵⁴ Matthias Raphael Stock⁵² Virginia Strati⁵⁶ Alexander
Studenikin⁶⁹ Jun Su²¹ Shifeng Sun¹² Xilei Sun¹¹ Yongjie Sun²³
Yongzhao Sun¹¹ Zhengyang Sun³¹ Narumon Suwonjandee⁷¹
Michal Szelezniak⁴⁵ Akira Takenaka³¹ Jian Tang²¹ Qiang Tang²¹
Quan Tang²⁴ Xiao Tang¹¹ Vidhya Thara Hariharan⁴⁹ Eric
Theisen⁵¹ Alexander Tietzsch⁵⁴ Igor Tkachev⁶⁸ Tomas Tmej⁴¹
Marco Danilo Claudio Torri⁵⁷ Francesco Tortorici⁵⁵ Konstantin
Treskov⁶⁷ Andrea Triossi⁶¹ Riccardo Trizzi^{61,60} Wladyslaw
Trzaska⁴² Yu-Chen Tung⁴⁰ Cristina Tuve⁵⁵ Nikita Ushakov⁶⁸
Vadim Vedin⁶⁵ Giuseppe Verde⁵⁵ Maxim Vialkov⁶⁹ Benoit
Viaud⁴⁷ Cornelius Moritz Vollbrecht^{50,48} Katharina von Sturm⁶¹
Vit Vorobel⁴¹ Dmitriy Voronin⁶⁸ Lucia Votano⁶³ Pablo Walker^{6,5}
Caishen Wang¹⁹ Chung-Hsiang Wang³⁹ En Wang³⁷ Guoli
Wang²² Jian Wang²³ Jun Wang²¹ Lu Wang¹¹ Meng Wang²⁴
Meng Wang²⁶ Ruiguang Wang¹¹ Siguang Wang¹³ Wei Wang²¹
Wenshuai Wang¹¹ Xi Wang¹⁷ Xiangyue Wang²¹ Yangfu Wang¹¹
Yaoguang Wang¹¹ Yi Wang¹¹ Yi Wang¹⁴ Yifang Wang¹¹
Yuanqing Wang¹⁴ Yuyi Wang¹⁴ Zhe Wang¹⁴ Zheng Wang¹¹
Zhimin Wang¹¹ Apimook Watcharangkool⁷² Wei Wei¹¹ Wei
Wei²⁶ Wenlu Wei¹¹ Yadong Wei¹⁹ Kaile Wen¹¹ Liangjian Wen¹¹
Jun Weng¹⁴ Christopher Wiebusch⁴⁸ Rosmarie Wirth⁴⁹ Bjoern
Wonsak⁴⁹ Diru Wu¹¹ Qun Wu²⁶ Yiyang Wu¹⁴ Zhi Wu¹¹ Michael
Wurm⁵¹ Jacques Wurtz⁴⁵ Christian Wysotski⁴⁸ Yufei Xi³²
Dongmei Xia¹⁸ Xiang Xiao²¹ Xiaochuan Xie²⁸ Yuguang Xie¹¹
Zhangquan Xie¹¹ Zhao Xin¹¹ Zhizhong Xing¹¹ Benda Xu¹⁴
Cheng Xu²⁴ Donglian Xu^{31,30} Fanrong Xu²⁰ Hangkun Xu¹¹ Jilei
Xu¹¹ Jing Xu⁹ Meihang Xu¹¹ Yin Xu³³ Yu Xu²¹ Baojun Yan¹¹
Qiyu Yan¹⁵ Taylor Yan⁷³ Xiongbo Yan¹¹ Yupeng Yan⁷³ Changgen
Yang¹¹ Chengfeng Yang²⁸ Jie Yang³⁷ Lei Yang¹⁹ Xiaoyu Yang¹¹
Yifan Yang¹¹ Yifan Yang² Haifeng Yao¹¹ Jiaxuan Ye¹¹ Mei Ye¹¹
Ziping Ye³¹ Frédéric Yermia⁴⁷ Zhengyun You²¹ Boxiang Yu¹¹
Chiye Yu¹⁹ Chunxu Yu³³ Guojun Yu²⁷ Hongzhao Yu²¹ Miao Yu³⁴

Xianghui Yu³³ **Zeyuan Yu**¹¹ **Zezhong Yu**¹¹ **Cenxi Yuan**²¹
Chengzhuo Yuan¹¹ **Ying Yuan**¹³ **Zhenxiong Yuan**¹⁴ **Baobiao**
Yue²¹ **Noman Zafar**⁶⁶ **Vitalii Zavadskyi**⁶⁷ **Shan Zeng**¹¹ **Tingxuan**
Zeng¹¹ **Yuda Zeng**²¹ **Liang Zhan**¹¹ **Aiqiang Zhang**¹⁴ **Bin Zhang**³⁷
Binting Zhang¹¹ **Feiyang Zhang**³⁰ **Haosen Zhang**¹¹ **Honghao**
Zhang²¹ **Jialiang Zhang**²⁷ **Jiawen Zhang**¹¹ **Jie Zhang**¹¹ **Jingbo**
Zhang²² **Jinnan Zhang**¹¹ **Mohan Zhang**¹¹ **Peng Zhang**¹¹ **Qingmin**
Zhang³⁵ **Shiqi Zhang**²¹ **Shu Zhang**²¹ **Shuihan Zhang**¹¹ **Siyuan**
Zhang²⁸ **Tao Zhang**³⁰ **Xiaomei Zhang**¹¹ **Xin Zhang**¹¹ **Xuantong**
Zhang¹¹ **Yinhong Zhang**¹¹ **Yiyu Zhang**¹¹ **Yongpeng Zhang**¹¹ **Yu**
Zhang¹¹ **Yuanyuan Zhang**³¹ **Yumei Zhang**²¹ **Zhenyu Zhang**³⁴
Zhijian Zhang¹⁹ **Jie Zhao**¹¹ **Rong Zhao**²¹ **Runze Zhao**¹¹ **Shujun**
Zhao³⁷ **Dongqin Zheng**²⁰ **Hua Zheng**¹⁹ **Yangheng Zheng**¹⁵
Weirong Zhong²⁰ **Jing Zhou**¹⁰ **Li Zhou**¹¹ **Nan Zhou**²³ **Shun**
Zhou¹¹ **Tong Zhou**¹¹ **Xiang Zhou**³⁴ **Jingsen Zhu**²⁹ **Kangfu Zhu**³⁵
Kejun Zhu¹¹ **Zihang Zhu**¹¹ **Bo Zhuang**¹¹ **Honglin Zhuang**¹¹
Liang Zong¹⁴ **Jiaheng Zou**¹¹ **Jan Züfle**⁵⁴ **Sebastian Zwickel**⁵²

¹Yerevan Physics Institute, Yerevan, Armenia

²Université Libre de Bruxelles, Brussels, Belgium

³Universidade Estadual de Londrina, Londrina, Brazil

⁴Pontifícia Universidade Católica do Rio de Janeiro, Rio de Janeiro, Brazil

⁵Millennium Institute for SubAtomic Physics at the High-energy Frontier (SAPHIR), ANID, Chile

⁶Pontificia Universidad Católica de Chile, Santiago, Chile

⁷Universidad Técnica Federico Santa María, Valparaíso, Chile

⁸Beijing Institute of Spacecraft Environment Engineering, Beijing, China

⁹Beijing Normal University, Beijing, China

¹⁰China Institute of Atomic Energy, Beijing, China

¹¹Institute of High Energy Physics, Beijing, China

¹²North China Electric Power University, Beijing, China

¹³School of Physics, Peking University, Beijing, China

¹⁴Tsinghua University, Beijing, China

¹⁵University of Chinese Academy of Sciences, Beijing, China

¹⁶Jilin University, Changchun, China

¹⁷College of Electronic Science and Engineering, National University of Defense Technology, Changsha, China

¹⁸Chongqing University, Chongqing, China

¹⁹Dongguan University of Technology, Dongguan, China

²⁰Jinan University, Guangzhou, China

²¹Sun Yat-Sen University, Guangzhou, China

²²Harbin Institute of Technology, Harbin, China

- ²³University of Science and Technology of China, Hefei, China
²⁴The Radiochemistry and Nuclear Chemistry Group in University of South China, Hengyang, China
²⁵Wuyi University, Jiangmen, China
²⁶Shandong University, Jinan, China, and Key Laboratory of Particle Physics and Particle Irradiation of Ministry of Education, Shandong University, Qingdao, China
²⁷Nanjing University, Nanjing, China
²⁸Guangxi University, Nanning, China
²⁹East China University of Science and Technology, Shanghai, China
³⁰School of Physics and Astronomy, Shanghai Jiao Tong University, Shanghai, China
³¹Tsung-Dao Lee Institute, Shanghai Jiao Tong University, Shanghai, China
³²Institute of Hydrogeology and Environmental Geology, Chinese Academy of Geological Sciences, Shijiazhuang, China
³³Nankai University, Tianjin, China
³⁴Wuhan University, Wuhan, China
³⁵Xi'an Jiaotong University, Xi'an, China
³⁶Xiamen University, Xiamen, China
³⁷School of Physics and Microelectronics, Zhengzhou University, Zhengzhou, China
³⁸Institute of Physics, National Yang Ming Chiao Tung University, Hsinchu
³⁹National United University, Miao-Li
⁴⁰Department of Physics, National Taiwan University, Taipei
⁴¹Charles University, Faculty of Mathematics and Physics, Prague, Czech Republic
⁴²University of Jyvaskyla, Department of Physics, Jyvaskyla, Finland
⁴³IJCLab, Université Paris-Saclay, CNRS/IN2P3, 91405 Orsay, France
⁴⁴University of Bordeaux, CNRS, LP2i, UMR 5797, F-33170 Gradignan, F-33170 Gradignan, France
⁴⁵IPHC, Université de Strasbourg, CNRS/IN2P3, F-67037 Strasbourg, France
⁴⁶Centre de Physique des Particules de Marseille, Marseille, France
⁴⁷SUBATECH, Université de Nantes, IMT Atlantique, CNRS-IN2P3, Nantes, France
⁴⁸III. Physikalisches Institut B, RWTH Aachen University, Aachen, Germany
⁴⁹Institute of Experimental Physics, University of Hamburg, Hamburg, Germany
⁵⁰Forschungszentrum Jülich GmbH, Nuclear Physics Institute IKP-2, Jülich, Germany
⁵¹Institute of Physics and EC PRISMA⁺, Johannes Gutenberg Universität Mainz, Mainz, Germany
⁵²Technische Universität München, München, Germany
⁵³Helmholtzzentrum für Schwerionenforschung, Planckstrasse 1, D-64291 Darmstadt, Germany
⁵⁴Eberhard Karls Universität Tübingen, Physikalisches Institut, Tübingen, Germany
⁵⁵INFN Catania and Dipartimento di Fisica e Astronomia dell'Università di Catania, Catania, Italy
⁵⁶Department of Physics and Earth Science, University of Ferrara and INFN Sezione di Ferrara, Ferrara, Italy
⁵⁷INFN Sezione di Milano and Dipartimento di Fisica dell'Università di Milano, Milano, Italy

- ⁵⁸INFN Milano Bicocca and University of Milano Bicocca, Milano, Italy
⁵⁹INFN Milano Bicocca and Politecnico of Milano, Milano, Italy
⁶⁰INFN Sezione di Padova, Padova, Italy
⁶¹Dipartimento di Fisica e Astronomia dell’Università di Padova and INFN Sezione di Padova, Padova, Italy
⁶²INFN Sezione di Perugia and Dipartimento di Chimica, Biologia e Biotecnologie dell’Università di Perugia, Perugia, Italy
⁶³Laboratori Nazionali di Frascati dell’INFN, Roma, Italy
⁶⁴University of Roma Tre and INFN Sezione Roma Tre, Roma, Italy
⁶⁵Institute of Electronics and Computer Science, Riga, Latvia
⁶⁶Pakistan Institute of Nuclear Science and Technology, Islamabad, Pakistan
⁶⁷Joint Institute for Nuclear Research, Dubna, Russia
⁶⁸Institute for Nuclear Research of the Russian Academy of Sciences, Moscow, Russia
⁶⁹Lomonosov Moscow State University, Moscow, Russia
⁷⁰Comenius University Bratislava, Faculty of Mathematics, Physics and Informatics, Bratislava, Slovakia
⁷¹Department of Physics, Faculty of Science, Chulalongkorn University, Bangkok, Thailand
⁷²National Astronomical Research Institute of Thailand, Chiang Mai, Thailand
⁷³Suranaree University of Technology, Nakhon Ratchasima, Thailand
⁷⁴Department of Physics and Astronomy, University of California, Irvine, California, USA

Abstract. The Jiangmen Underground Neutrino Observatory (JUNO), the first multi-kton liquid scintillator detector, which is under construction in China, will have a unique potential to perform a real-time measurement of solar neutrinos well below the few MeV threshold typical for Water Cherenkov detectors. JUNO’s large target mass and excellent energy resolution are prerequisites for reaching unprecedented levels of precision. In this paper, we provide estimation of the JUNO sensitivity to ^7Be , *pep*, and CNO solar neutrinos that can be obtained via a spectral analysis above the 0.45 MeV threshold. This study is performed assuming different scenarios of the liquid scintillator radiopurity, ranging from the most optimistic one corresponding to the radiopurity levels obtained by the Borexino experiment, up to the minimum requirements needed to perform the neutrino mass ordering determination with reactor antineutrinos — the main goal of JUNO. Our study shows that in most scenarios, JUNO will be able to improve the current best measurements on ^7Be , *pep*, and CNO solar neutrino fluxes. We also perform a study on the JUNO capability to detect periodical time variations in the solar neutrino flux, such as the day-night modulation induced by neutrino flavor regeneration in Earth, and the modulations induced by temperature changes driven by helioseismic waves.

Contents

1 JUNO experiment	3
2 Solar neutrinos	4
2.1 Solar neutrinos production and propagation	4
2.2 Solar neutrinos detection in JUNO	6
3 Backgrounds	6
3.1 Internal backgrounds	8
3.2 External backgrounds	9
3.3 Cosmogenic backgrounds	9
3.3.1 Identification of ^{11}C : the TFC algorithm	11
3.4 Background from reactor anti-neutrinos	12
4 Strategy and methods for solar neutrino spectroscopy	12
4.1 Production of reference energy distribution (PDFs)	12
4.2 Toy dataset generation	13
4.3 Multivariate fit	13
5 Solar neutrino spectroscopy	14
5.1 Sensitivity on ^7Be neutrinos	15
5.2 Sensitivity on <i>pep</i> neutrinos	18
5.3 Sensitivity on CNO neutrinos	19
5.4 Sensitivity results on ^{13}N and ^{15}O neutrinos	22
6 Periodic modulations of the ^7Be neutrino rate	23
6.1 Sensitivity to solar neutrino day-night asymmetry	24
6.1.1 The statistical subtraction method	24
6.1.2 The Lomb Scargle Method	25
6.1.3 Results	26
6.2 Sensitivity to g-modes	27
7 Conclusions	28

Introduction

Solar neutrinos, emitted in fusion processes powering our star, bring us information about the energy-production mechanism in the Sun as well as about the chemical composition of the solar core. In spite of their copious flux at Earth (about $6 \times 10^{10} \nu \text{cm}^{-2}\text{s}^{-1}$), detecting solar neutrinos is experimentally challenging: it requires large volume detectors and low-background environment. Nonetheless, the study of solar neutrinos has been very rewarding: on one hand, it has provided a confirmation of the Standard Solar Model (SSM) flux predictions [1]; on the other hand, it has proven that neutrinos oscillate (and therefore have mass), it has allowed to determine the oscillation parameters Δm_{12}^2 and θ_{12} [2] and to probe new physics beyond the Standard Model [3].

Solar neutrinos have been originally studied by radiochemical experiments (Homestake [4], Gallex [5], GNO [6], and SAGE [7]) and by large water Cherenkov detectors (Kamiokande [8], Super-Kamiokande [9], and SNO [10]). However, both techniques are actually sub-optimal for this task: the first one provides no other information but counting of events; the second one imposes a high energy threshold of several MeV and has an intrinsically low energy resolution. Borexino [11] has proven that the liquid scintillator technique is a suitable tool to study solar neutrinos with a low energy threshold, thanks to the good energy and position resolutions, and the pulse-shape discrimination capability. Borexino has performed a complete spectroscopy of solar neutrinos coming both from the “proton-proton” (*pp*) chain [12], which provides about 99% of the solar energy, and the CNO cycle [13, 14]. Recently, Borexino also developed a Correlated Integrated Directionality (CID) method exploiting the sub-dominant Cherenkov light in order to disentangle a solar neutrino signal from an isotropic background [15, 16].

Several experiments, such as Borexino, SNO, and Super-Kamiokande have also studied periodic variations of the solar neutrino flux over time, both the seasonal modulation caused by the eccentricity of the Earth’s orbit [17–19] and the day-night effect induced by neutrino-matter interactions with the Earth during the night [20–22].

Despite these achievements, there are still open topics in solar and neutrino physics that could be investigated by the next generation of solar neutrino experiments, like the solar metallicity problem [23] or possible neutrino non standard interactions [24].

The Jiangmen Underground Neutrino Observatory (JUNO), a multi-kton liquid scintillator detector under construction in China, could potentially be a decisive player in this game, thanks to its high mass and energy resolution, provided the radioactive background is kept under control and the detector response is fully understood. The JUNO potential to detect ^8B solar neutrinos with unprecedented 2 MeV threshold and to test the survival probability of the upturn region has already been discussed in [25, 26]. In this article, we explore the sensitivity of JUNO to intermediate energy solar neutrinos, *i.e.* ^7Be , *pep*, and CNO as a function of different possible experimental scenarios (mainly radiopurity and exposure). These neutrinos represent a large fraction of the total flux from the Sun. In order to avoid the problem of ^{14}C and ^{14}C pile-up which is dominant at low energies, we restrict our analysis to the energy range (0.45–1.6) MeV. For this reason, we don’t discuss *pp* neutrinos.

The structure of this article is as follows: Section 1 describes the main characteristics of the JUNO detector design and its expected performance. Section 2 is dedicated to solar neutrinos production and propagation mechanisms and their detection in JUNO. The classification of backgrounds relevant for this study and the definitions of various radiopurity scenarios considered are discussed in Section 3. The analysis strategy and methods adopted

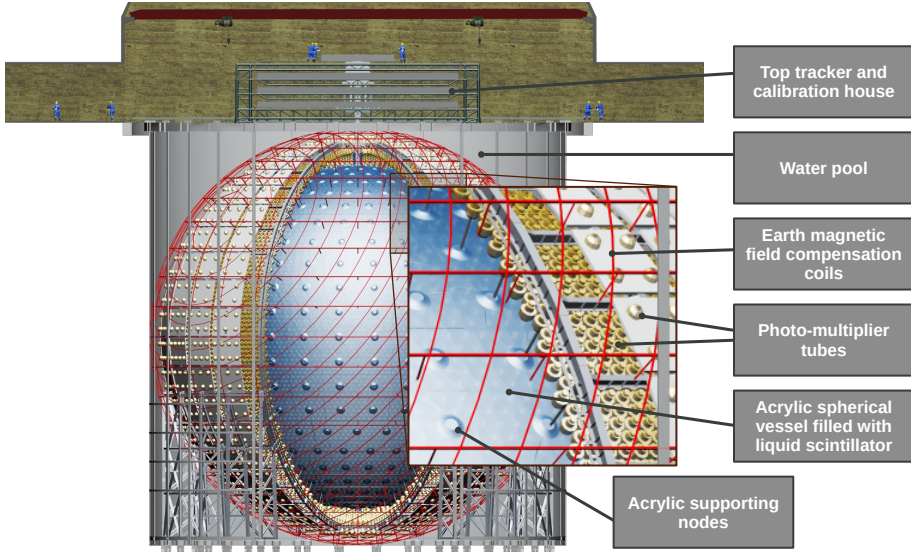


Figure 1. Schematic drawing of the main JUNO detector.

for the sensitivity studies are discussed in Section 4, while the sensitivity to ${}^7\text{Be}$, *pep*, and CNO solar neutrinos is given in Section 5. In Section 6, the JUNO potential to detect periodic modulations of the ${}^7\text{Be}$ solar neutrino flux is studied with the focus on short-term modulations, as well as on the day-night effect. Finally, the summary and outlook of this work is given in Section 7.

1 JUNO experiment

The JUNO experiment [27] is based on a liquid scintillator detector currently under construction in an underground laboratory with a vertical overburden of $\approx 650\text{ m}$ ($\approx 1800\text{ m}$ water equivalent) in Jiangmen city in Southern China. The JUNO detector is located at a distance of 52.5 km from both the Yangjiang and the Taishan nuclear power plants. This baseline is optimized for the JUNO primary goal, *i.e.* the determination of the neutrino mass ordering via the interplay between the fast and slow oscillation pattern of the reactor anti-neutrinos spectrum¹ [28, 29] also exploiting a reference spectrum provided by TAO [30]. To achieve this, JUNO requires a large target mass and an excellent energy resolution, which offers further opportunities for a variety of topics in the areas of neutrino and astroparticle physics [29, 31–35].

A sketch of the JUNO detector is shown in Fig. 1. It consists of a Central Detector (CD), containing 20 kton of liquid scintillator mixture in an acrylic sphere of 17.7 m radius and 120 mm thickness. The liquid scintillator mixture has been optimized in dedicated studies with a Daya Bay detector [36]; it will be mainly composed of linear alkylbenzene (LAB) and will also contain 2.5 g/L of 2,5-diphenyloxazole (PPO), which will act as scintillation fluor and 3 mg/L of p-bis-(*o*-methylstyryl)-benzene (bis-MSB), which will act as wavelength shifter. The light attenuation length is greater than 20 m at 430 nm in order to make up for the huge

¹Reactor antineutrinos $\bar{\nu}_e$ are detected via the Inverse Beta Decay (IBD) reaction on protons ($\bar{\nu}_e + p \rightarrow e^+ + n$), which provides an excellent tool to identify the signal via the space-time coincidence of the *prompt* (e^+) and *delayed* (2.2 MeV gamma following the neutron capture on a proton) signals.

CD dimensions. Before filling, the liquid scintillator will be purified to improve its radiopurity and a pre-detector (OSIRIS) will monitor it [37]. The acrylic vessel is supported by a spherical stainless steel (SS) structure via 590 connecting bars. The scintillation light emitted due to the energy depositions in liquid scintillator is detected by 17,612 20-inch PMTs and 25,600 3-inch PMTs mounted on the SS structure facing the acrylic sphere. This provides a large photo coverage (75.2% for 20-inch PMTs and 2.7% for 3-inch PMTs), which is necessary to collect a large number of photoelectrons per unit of deposited energy, leading to an unprecedented energy resolution for a liquid scintillator detector of $\approx 3\% \sqrt{E(\text{MeV})}$ at the price of a large dark noise rate of about 30 kBq.

The CD is submerged in a cylindrical water pool (WP) of 43.5 m diameter and height of 44.0 m, filled with 35 kton of ultra-pure water. The WP shields the CD against external fast neutrons and gammas. It also acts as a Cherenkov veto for cosmic muons having a flux of about $0.004 \text{ m}^{-2}\text{s}^{-1}$ and a mean energy of 207 GeV. The muons passing through water produce Cherenkov light detected by 2,400 20-inch PMTs installed on the outer surface of SS structure. The SS structure has inner diameter of 40.1 m with 30 pairs of legs attached to the floor of WP. The WP walls and a SS support structure are coated using Tyvek reflective foil to increase light collection efficiency. On the top of the WP, a Top Tracker (TT) is placed to precisely measure the tracks of a sub-sample of the crossing muons. It consists of a plastic scintillator array formerly used in the Target Tracker of the OPERA experiment [38].

Multiple calibration systems based on different radioactive and laser-based sources have been designed and developed to calibrate the detector and to correct for the non-uniformity and non-linearity of its response with better than 1% precision. The calibration operation will be carried out through an acrylic chimney, which connects the CD to the outside from the top. The details regarding the calibration systems and strategies can be found in [39].

2 Solar neutrinos

This section describes solar neutrinos, starting from their production in the Sun’s core up to their detection and expected interaction rates in the JUNO detector.

2.1 Solar neutrinos production and propagation

Solar neutrinos are originated with electron flavour (ν_e) in the hydrogen-to-helium fusion reactions occurring in the Sun’s core. This fusion can proceed via two distinct mechanisms: the dominant proton-proton (pp) chain and the sub-dominant CNO cycle. In the latter process, the elements Carbon, Nitrogen, and Oxygen catalyze the fusion. The CNO cycle contributes only $\approx 1\%$ to the solar energy production, with a large uncertainty due to a poor knowledge of the Sun’s metallicity, *i.e.* abundance of elements heavier than Helium. However, it is expected that the CNO fusion is the primary energy producing process in the stars whose mass is at least 1.3 times bigger than the solar mass [1, 40–42].

The solar neutrinos produced in a given reaction belonging either to the pp chain or the CNO cycle exhibit a characteristic energy spectrum as shown in Fig. 2. The flux of solar neutrinos is by far dominated by pp neutrinos ($\approx 6 \times 10^{10} \text{ cm}^{-2}\text{s}^{-1}$), which are produced in the primary reaction of the pp -chain and have a maximum energy of 0.42 MeV. The pp -chain produces also ^7Be , pep , ^8B , and hep neutrinos. The ^7Be are mono-energetic neutrinos with two distinct lines at 0.862 MeV and 0.384 MeV with a production branching ratio of 0.8949 and 0.1052, respectively. The overall flux of ^7Be neutrinos is $\approx 5 \times 10^9 \text{ cm}^{-2}\text{s}^{-1}$. The pep neutrinos are also mono-energetic (1.44 MeV) with a flux of $\approx 1.4 \times 10^8 \text{ cm}^{-2}\text{s}^{-1}$.

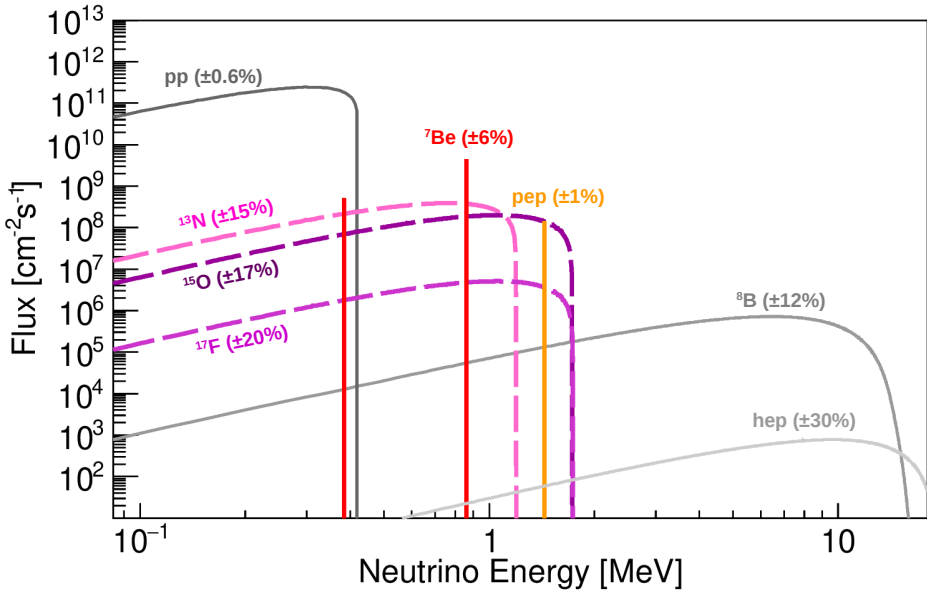


Figure 2. Energy spectra of solar neutrinos from the *pp* chain (solid lines) and CNO cycle (dashed lines). The coloured lines indicate the “intermediate energy” solar neutrinos which are the subject of this paper. The spectral shapes are taken from <http://www.sns.ias.edu/~jnb/> and flux normalization from the HZ-SSM predictions given in [1]. The flux (vertical scale) is given in units of $\text{cm}^{-2}\text{s}^{-1}\text{MeV}^{-1}$ for continuum sources and in $\text{cm}^{-2}\text{s}^{-1}$ for monoenergetic sources. The values in parenthesis show the corresponding relative uncertainties of the SSM predictions.

The ^8B neutrinos are characterised by a low flux ($\approx 5 \times 10^6 \text{ cm}^{-2} \text{ s}^{-1}$) and a spectrum that extends up to about 16.5 MeV. The *hep* neutrinos extend to slightly higher energy than ^8B neutrinos, however, their flux is so low that they have not been yet experimentally confirmed. The neutrinos from CNO cycle with a flux similar to that of *pep* neutrinos have an energy spectrum extending up to 1.74 MeV, taking into account the contributions from ^{13}N , ^{15}O , and ^{17}F decays. The analysis presented in this work is focused on ^7Be , *pep*, and CNO neutrinos. The studies regarding CNO neutrinos are performed in two different ways. Firstly, we consider CNO as a single species representing a weighted sum of all three components according to the SSM predictions. Secondly, we consider individually ^{13}N and ^{15}O components, where the latter includes also sub-dominant ^{17}F neutrinos having a degenerate energy spectrum with ^{15}O .

The *Standard Solar Model* describes a star with one solar mass in hydrostatic equilibrium. The model is calibrated to satisfy constraints imposed by the present day solar luminosity, radius, mass, and surface metal-to-Hydrogen abundance ratio (Z/X , referred to as solar metallicity). Solar neutrino fluxes are an output of the SSM together with other relevant observables, like for example, the sound speed profiles on the Sun surface: note that helioseismology provides experimental data on these [43]. The newest generation of SSMs is called B16 [1]. The solar metal abundances can be measured experimentally through spectroscopy of the solar surface. However, during the past two decades, the analysis of the spectroscopic data has led to controversial results, the so-called low-metallicity (LZ) [44, 45] and high-metallicity (HZ) measurements [23, 46]. It should be noted that SSMs using in input the low-metallicity

values fail to reproduce helioseismological measurements, while high-metallicity ones are in better agreement with them [1, 23].

An important step towards the solution of this problem might come from the precise measurements of solar neutrino fluxes, especially of CNO neutrinos. In fact the predictions of the HZ and LZ models for ${}^7\text{Be}$, ${}^8\text{B}$, and CNO differ by 8.9%, 17.6%, and 30%, respectively. This is because metallicity influences the plasma opacity of the Sun, which consequently impacts the temperature of the Sun and the fusion rates. Additionally, the flux of CNO neutrinos is also affected directly by the abundance of its catalyzing metals: Carbon, Nitrogen, and Oxygen. Table 1 summarizes the fluxes of ${}^7\text{Be}$, *pep*, and CNO neutrinos as predicted by the LZ-SSM and HZ-SSM [1].

The electron flavour solar neutrinos undergo the process of flavour transformation particularly during their propagation through the dense solar matter due to coherent forward scattering off electrons present in the Sun. This is known as the *Mikheyev–Smirnov–Wolfenstein* (MSW) effect [47, 48]. The survival probability (P_{ee}) is dominated by vacuum oscillations below 1 MeV ($P_{ee} \approx 0.54$) while it is matter-dominated for energies greater than 8 MeV ($P_{ee} \approx 0.32$) with a smooth transition occurring for intermediate energies [2, 49].

2.2 Solar neutrinos detection in JUNO

In JUNO, solar neutrinos of all flavors are detected by means of elastic scattering off electrons:

$$\nu_x + e^- \rightarrow \nu_x + e^- \quad x = e, \mu, \tau, \quad (2.1)$$

that has no intrinsic energy threshold. The cross section for electron neutrinos (ν_e) is about six times larger than that for non-electron neutrinos (ν_μ and ν_τ), since only for ν_e the interaction can proceed also via the charge current interaction. In this elastic scattering process, only a fraction of the neutrino energy E_ν is transferred to the electron, which recoils and transfers the gained kinetic energy E_{kin} to the scintillator, producing scintillation light. This *visible energy* (E_{vis}) is to first order linearly dependent on E_{kin} . Due to the kinematics of the scattering process, a continuous electron recoil spectrum is obtained even in case of a mono-energetic neutrino source such as ${}^7\text{Be}$ and *pep* neutrinos. In addition, the directional information is almost completely lost due to the fact that the isotropic scintillation light is dominant over the directional Cherenkov light, which contributes only at the sub-percent level.

The interaction rates of ${}^7\text{Be}$, *pep*, and CNO neutrinos expected in JUNO according to the predictions of HZ-SSM and LZ-SSM can be found in Tab. 1. This calculation makes use of the SSM flux prediction [1] and oscillation parameters [2] together with the electron number density in the liquid scintillator of $3.38 \times 10^{32} e^-/\text{kton}$. The table shows also the expected rates for the range $0.45 \text{ MeV} < E_{\text{vis}} < 1.6 \text{ MeV}$, the energy range of interest (ROI) used in this analysis to optimize the signal-to-noise ratio.

3 Backgrounds

To reach its ambitious physics goals, JUNO needs to keep radiopurity at very high levels. This is especially true for the solar neutrino analysis, where neutrino elastic scattering events are indistinguishable on an event-by-event basis from the background ones, since all of them consist of a single flash of light and no coincidence technique can be applied (contrary to what happens in the IBD reaction used for reactor antineutrino detection). Furthermore, the scintillation light is isotropic and the directional information cannot be exploited to separate signal from background. For these reasons, the sensitivity of JUNO to solar neutrinos

	Solar ν	^7Be	pep	CNO
HZ-SM	$\Phi [10^8 \text{ cm}^{-2} \text{ s}^{-1}]$	$49.3(1 \pm 0.06)$	$1.44(1 \pm 0.009)$	$4.88(1 \pm 0.11)$
	$R [\text{cpd/kton}]$	489 ± 29	28.0 ± 0.4	50.3 ± 8.0
	$R^{\text{ROI}} [\text{cpd/kton}]$	142.5 ± 8.3	17.1 ± 0.2	16.6 ± 2.6
LZ-SM	$\Phi [10^8 \text{ cm}^{-2} \text{ s}^{-1}]$	$45.0(1 \pm 0.06)$	$1.46(1 \pm 0.009)$	$3.51(1 \pm 0.10)$
	$R [\text{cpd/kton}]$	447 ± 26	28.4 ± 0.4	36.0 ± 5.3
	$R^{\text{ROI}} [\text{cpd/kton}]$	130.0 ± 7.5	17.3 ± 0.2	11.9 ± 1.8
Borexino results	$\Phi [10^8 \text{ cm}^{-2} \text{ s}^{-1}]$	$49.9 \pm 1.1^{+0.6}_{-0.8}$	$1.27 \pm 0.19^{+0.08}_{-0.12} (\text{LZ})$ $1.39 \pm 0.19^{+0.08}_{-0.13} (\text{HZ})$	$6.6^{+2.0}_{-0.9}$

Table 1. Fluxes Φ and interaction rates R in the entire energy range for ^7Be , pep , and CNO solar neutrinos. The first and second rows show B16-SSM [1] predicted fluxes and corresponding expected rates in JUNO according to the HZ and LZ hypothesis, respectively. The expected rates R^{ROI} between $0.45 \text{ MeV} < E_{\text{vis}} < 1.6 \text{ MeV}$, which is the energy range of interest (ROI) chosen in this analysis, is also shown. The last row reports the current best experimental results for ^7Be and pep [12] and CNO [14] neutrinos obtained by the Borexino experiment (note that the pep results slightly depend on the HZ/LZ SSM predictions used for constraining CNO neutrino flux in the fit). All the rates are reported in cpd/kton units, which are counts per day per kton of scintillator.

is intertwined with the amount and type of backgrounds present in the detector. The relevant backgrounds can be classified into three categories: *i*) *internal background* from the radioactive decays of contaminants of the scintillator itself, *ii*) *external background* due to radioactivity in the materials surrounding the scintillator, and *iii*) *cosmogenic background* related to cosmic muons crossing the detector.

The strategy to control internal background due to radioactivity is described in detail in [50]. It is mainly based on the careful selection of materials and on a multi-step purification procedure of the JUNO liquid scintillator, which include distillation (to remove heavy metals and improve the transparency), water extraction (to remove radioisotopes from U/Th chains and ^{40}K), and steam stripping (to remove gaseous impurities, such as ^{85}Kr and ^{222}Rn). Even though the preliminary results of the prototype plants are very promising, the actual levels of contamination, which will be eventually reached, are still not known. In the following paragraphs we describe the assumptions for our sensitivity studies for all types of backgrounds.

Differently from the internal background, the external background is not uniform inside the LS. This is due to the JUNO onion-like shielding structure, composed by concentric layers of materials with increasing radiopurity when going towards the center.

Cosmic muons and cosmogenic backgrounds are significantly reduced by the fact that the detector is located underground. Furthermore, the residual muons will be effectively detected and tracked, using not only the CD but also the dedicated WP and TT sub-detectors.

Type	Isotope	\mathcal{Q} (MeV)	Mean Life	Decay mode
Internal	^{85}Kr	0.687	15.4 y	β^-
	^{40}K (BR=89%)	1.31	1.85×10^9 y	β^-
	^{40}K (BR=11%)	1.46	1.85×10^9 y	e^- capture + γ
	^{232}Th chain	8.8	2.03×10^{10} y	α, γ, β^-
	^{238}U chain	7.8	6.45×10^9 y	α, γ, β^-
	^{210}Pb	0.063	32.2 y	γ, β^-
	^{210}Bi	1.16	7.23 d	β^-
Cosmogenic	^{210}Po	5.4	200 d	α
	^{11}C	1.98	29.4 min	β^+
	^{10}C	3.65	27.8 s	β^+
	^6He	3.51	1.1 s	β^-

Table 2. Summary of the internal and cosmogenic backgrounds relevant for the ^7Be , *pep*, and CNO solar neutrinos analysis. Note that for the ^{232}Th and ^{238}U chains, we report the lifetime of the parent isotope of the decay chain, and the highest \mathcal{Q} value of the chain isotopes.

3.1 Internal backgrounds

The events generated by the decay of radioactive isotopes contained inside the scintillator are known as internal backgrounds. In the ROI considered in this paper, the relevant radioactive isotopes are ^{40}K , ^{85}Kr , the ^{232}Th chain, the ^{238}U chain and the ^{210}Pb chain ($^{210}\text{Pb} \rightarrow ^{210}\text{Bi} \rightarrow ^{210}\text{Po}$) as shown in Tab. 2. We have performed our sensitivity studies assuming four scenarios for these isotopes concentrations (see Tab. 3):

1. The *IBD* scenario corresponds to the minimum radiopurity requirements needed for the neutrino mass ordering measurement [37]. We recall that the mass ordering analysis will exploit the coincidence of two events in sequence, therefore a higher rate of background events can be tolerated. Preliminary tests performed with the purification plant prototypes demonstrate that the IBD radiopurity scenario can be reached.
2. The *baseline* scenario corresponds to a factor 10 improvement with respect to the *IBD* scenario for all isotopes. It is not guaranteed that the purification plants will be able to bring the scintillator down to these radiopurity levels. However, it is not possible to test this directly before the JUNO data taking, since we don't have enough sensitivity to detect these low levels of contaminants.
3. The *ideal* scenario corresponds to a factor 10 improvement with respect to the *baseline* scenario for all isotopes, except for ^{210}Pb and ^{85}Kr for which the improvement is only of a factor 5.
4. The *Borexino-like* scenario (also abbreviated as BX-like) corresponds to the radiopurity levels reached on ^{40}K , ^{85}Kr , ^{232}Th chain and ^{238}U chain by the Borexino experiment in

Phase-III in the Fiducial Volume [12, 13, 51]. Note that this scenario is considered only as a best-case scenario reference, since the JUNO central detector size would make it very difficult (if not impossible) to reach this level of radiopurity.

The list of all contaminants, with their concentration and corresponding count rate in JUNO for each radiopurity scenario, can be found in Tab. 3. We provide in this table the count rate without assuming any energy threshold (R) and in the ROI (R^{ROI}).

Note that in this table, we also include ^{210}Pb which belongs to the ^{238}U chain, but is often found out of equilibrium with respect to the other elements of the chain [52, 53]. While the additional ^{210}Pb contribution is not a problem, since its end-point energy ($Q_{\text{Pb}} = 63.5 \text{ keV}$) is well below the ROI, the isotopes produced in its decay chain, *i.e.* ^{210}Bi and ^{210}Po , represent a major source of background especially for the *pep* and CNO measurements.

Also the isotope ^{210}Po could be out of equilibrium with both the ^{238}U and the ^{210}Pb chains. We don't include this contribution in the table, but we study this case separately in Section 5.1.

The background list in Tab. 3 doesn't include pileup, that is, the superposition of two or more events within the same acquisition window. Depending on the actual levels of radiopurity, pileup events (mainly due to multiple ^{14}C events or a combination of a ^{14}C event with the most common backgrounds) could be potentially dangerous for the solar neutrino analysis and should be taken into account in the spectral fit procedure. However, it would mainly affect the lower energy portion of the spectrum. In the analysis described in this paper, we have chosen the energy threshold in such a way as to minimize the contribution of this background: in these conditions, our simulations show that in all four radiopurity scenarios pileup has a negligible impact, provided we are able to constrain both its rate and shape in the analysis. This can be done by estimating the pileup features independently from the spectral fit, both with dedicated Monte Carlo simulations or with data-driven methods [54]. For the current studies, we have not included pileup in our sensitivity studies.

3.2 External backgrounds

The main external background in JUNO is the γ radioactivity of the materials that surround the scintillator (PMTs, SS structure, and acrylic vessel), mainly ^{208}Tl , ^{214}Bi , and ^{40}K isotopes in the PMT glass with their typical energy range of 1–3 MeV. Monte Carlo simulations show that a spherical fiducial volume (FV) of radius $r_{\text{FV}} \lesssim 15 \text{ m}$ would be large enough to completely suppress the external γ contributions [25, 50]. To be conservative, only events occurring inside a sphere of $r_{\text{FV}} < 14 \text{ m}$ are included in the analysis. For this reason, external background will be neglected in the following.

3.3 Cosmogenic backgrounds

Cosmogenic isotopes are created by the spallation of cosmic muons on carbon atoms inside the liquid scintillator. Many of them are short-lived and can be fully removed by a simple time veto cut around the muon track. This cut will introduce a dead time which is currently not taken into account in our analysis. The relevant cosmogenic isotopes surviving the above mentioned cuts are ^{11}C , ^{10}C , and ^{6}He , which are long-lived isotopes decaying in the energy region of interest with non-negligible rates. The cosmogenic isotope rate can be predicted by scaling the reference experimental measurements from KamLAND [55] and Borexino [56, 57]:

	^{40}K	^{85}Kr	^{232}Th chain	^{238}U chain	^{210}Pb chain
IBD radiopurity scenario					
$c \left[\frac{\text{g}}{\text{g}} \right]$	1×10^{-16}	4×10^{-24}	1×10^{-15}	1×10^{-15}	5×10^{-23}
$R \left[\frac{\text{cpd}}{\text{kton}} \right]$	2289	5000	3508	15047	36817
$R^{\text{ROI}} \left[\frac{\text{cpd}}{\text{kton}} \right]$	1562	705	2100	7368	17269
Baseline radiopurity scenario					
$c \left[\frac{\text{g}}{\text{g}} \right]$	1×10^{-17}	4×10^{-25}	1×10^{-16}	1×10^{-16}	5×10^{-24}
$R \left[\frac{\text{cpd}}{\text{kton}} \right]$	229	500	351	1505	3682
$R^{\text{ROI}} \left[\frac{\text{cpd}}{\text{kton}} \right]$	156	70	210	737	1727
Ideal radiopurity scenario					
$c \left[\frac{\text{g}}{\text{g}} \right]$	1×10^{-18}	8×10^{-26}	1×10^{-17}	1×10^{-17}	1×10^{-24}
$R \left[\frac{\text{cpd}}{\text{kton}} \right]$	23	100	35	150	736
$R^{\text{ROI}} \left[\frac{\text{cpd}}{\text{kton}} \right]$	16	14	21	74	345
Borexino-like radiopurity scenario					
$c \left[\frac{\text{g}}{\text{g}} \right]$	2×10^{-19}	8×10^{-26}	5.7×10^{-19}	9.4×10^{-20}	5×10^{-25}
$R \left[\frac{\text{cpd}}{\text{kton}} \right]$	4.2	100	2	1.4	347
$R^{\text{ROI}} \left[\frac{\text{cpd}}{\text{kton}} \right]$	2.9	14	1	1	163

Table 3. Summary of internal background contributions for ^7Be , *pep*, and CNO solar neutrinos analysis in different radiopurity scenarios, without assuming any energy threshold (R) and in the ROI (R^{ROI}). The rates for the ^{232}Th and ^{238}U chains are obtained summing up the contributions of all daughters in the chain. The last column reports the contribution of ^{210}Pb assuming it will be out-of-equilibrium with respect to the ^{238}U chain. Note that in the so-called Borexino scenario the ^{40}K , ^{232}Th , and ^{238}U contaminations are set to the upper limit found by Borexino [12, 13, 51].

$$R^{\text{JUNO}} = R^{\text{ref}} \cdot \left(\frac{\bar{E}_\mu^{\text{JUNO}}}{\bar{E}_\mu^{\text{ref}}} \right)^\alpha \cdot \frac{\Phi(\mu)^{\text{JUNO}}}{\Phi(\mu)^{\text{ref}}} \cdot \frac{\epsilon_C^{\text{JUNO}}}{\epsilon_C^{\text{ref}}}, \quad (3.1)$$

where \bar{E}_μ is the average muon energy at the corresponding experimental site, $\alpha = 0.703 \pm 0.002$ is the spectral index of the energy dependence of the isotope production yield as measured

Isotope	$R_{\text{Scaling exp.}}$ [cpd/kton]	R [cpd/kton]	$\langle R \rangle$ [cpd/kton]	$\langle R \rangle_{\text{ROI}}$ [cpd/kton]
^{11}C	$R_{\text{Bx}} = 274 \pm 3$ $R_{\text{KL}} = 1106 \pm 8$	1890 ± 199 1959 ± 254	1916 ± 157	1761 ± 144
^{10}C	$R_{\text{Bx}} = 6.2 \pm 2.2$ $R_{\text{KL}} = 21.1 \pm 1.8$	41.4 ± 15.3 36.5 ± 5.7	37.1 ± 5.3	0.25 ± 0.04
^6He	$R_{\text{Bx}} = 11.1 \pm 4.5$ $R_{\text{KL}} = 15.4 \pm 2$	74 ± 31 26.6 ± 4.9	27.8 ± 4.8	12.7 ± 2.19

Table 4. Summary of cosmogenic background contributions for ^7Be , pep , and CNO solar neutrinos analysis. The interaction rates of cosmogenic backgrounds in KamLAND (R_{KL}) [55] and Borexino (R_{Bx}) Phase-I [56, 57] are reported in the first column. The expected JUNO production rate evaluated by means of the scaling method (Eq. 3.1), by exploiting the Borexino and KamLAND results separately, are displayed in the second column. The rates assumed in this analysis, without assuming any energy threshold ($\langle R \rangle$) and in the ROI ($\langle R \rangle_{\text{ROI}}$), are reported in the third and fourth column respectively.

by KamLAND, $\Phi(\mu)$ is the incoming total muon flux, and ϵ_C is the mass fraction of carbon atoms. The selection efficiencies of all three experiments are assumed to be comparable. For JUNO, the value of \bar{E}_μ , $\Phi(\mu)$, and ϵ_C are 209.2 ± 6.4 GeV, 10.8 ± 1.1 m $^{-2}$ h $^{-1}$, and 0.8792 respectively. The expected production rates evaluated by means of the scaling method (Eq. 3.1), by exploiting the Borexino and KamLAND results separately, are displayed in the second column of Tab. 4. For each cosmogenic isotope, the weighted average of these rates is used to calculate the JUNO expected cosmogenic rates: the values, in the full energy range and in the ROI ($\langle R \rangle$ and $\langle R \rangle_{\text{ROI}}$), are reported in the last two columns.

3.3.1 Identification of ^{11}C : the TFC algorithm

Due to their long lifetimes, the events from ^{11}C , ^{10}C , and ^6He backgrounds cannot be removed by a simple detector veto. Fortunately, the spallation reaction by the parent muon is followed by a cosmogenic decay and a neutron capture, which allows us to use so-called Three-Fold-Coincidence (TFC) algorithm [58]. By exploiting the spatial and time coincidence of those events, this method identifies space-time regions where the creation of cosmogenic backgrounds is highly probable: typically, the selected regions are a cylinder around the muon track and spheres around the point where the γ from the neutron capture is reconstructed. Based on this, the JUNO solar neutrino dataset is split into two complementary data samples: *TFC-tagged* and *TFC-subtracted*. The performance of this algorithm is mainly driven by two parameters:

- *Tagging Power* (TP), defined as the percentage of correctly identified cosmogenic background events;
- *Subtracted-dataset Exposure* (SE), representing the remaining exposure in the TFC-subtracted dataset after the TFC application.

To date, no such method has been developed specifically for the JUNO experiment. So, the values of these two parameters chosen are TP = 0.9 and SE = 0.7, assuming similar performances to the working values used in Borexino [12, 58]. The impact of different values of TP and SE on the JUNO sensitivity to ^7Be , pep , and CNO neutrinos is discussed in Section 5.

3.4 Background from reactor anti-neutrinos

Assuming a 26.6 GW reactor thermal power and a baseline of 52.5 km, the flux of reactor anti-neutrinos at the JUNO detector is $\approx 1.5 \times 10^7 \text{ cm}^{-2}\text{s}^{-1}$. We estimate the rate of background events induced by $\bar{\nu}_e$ through elastic scattering process to be 1.4 cpd/kton in the entire energy range and 1.3 cpd/kton for visible energy $E_{\text{vis}} < 2 \text{ MeV}$. This calculation was performed using the $\bar{\nu}_e$ spectrum and the fission fraction from [59] and their energy released per fission from [60]. When compared to the expected rate of solar neutrinos, radioactive and cosmogenic backgrounds, the contribution from anti-neutrinos can be considered negligible; hence, it is not included in the presented studies.

4 Strategy and methods for solar neutrino spectroscopy

In a liquid scintillator, the signal induced by solar neutrinos which scatter off electrons is generally indistinguishable on an event-by-event basis from the ones produced by radioactive and cosmogenic backgrounds. However, it is possible to extract the neutrino signal by fitting the energy distribution of detected events, modeled as the sum of neutrino and background contributions. The fit requires in input the expected energy distributions, that is a Probability Density Function (PDF), of each background and signal component and returns in output the corresponding contributing amplitude (number of events). This strategy, which has been successfully adopted for solar neutrino spectroscopy by Borexino [12, 13, 52], will be even more efficient in JUNO thanks to its excellent energy resolution and its large mass. The fit is simultaneously performed on two complementary partitions of the available dataset: the so-called TFC-subtracted one, depleted in ^{11}C by means of the Three-Fold-Coincidence technique (see Sec. 3.3), and the complementary TFC-tagged one, more populated in ^{11}C . The reference PDFs for the signal and backgrounds used in the fit are obtained from complete Monte Carlo simulations of the JUNO detector.

In the following, we describe in detail the fundamental steps for these sensitivity studies: the production of the reference energy distribution for each background and signal species (Sec. 4.1), the production of toy datasets (Sec. 4.2), and the fit to extract the contribution of every background and signal species (Sec. 4.3). Note that this analysis assumes a perfect knowledge of the detector energy response and of the theoretical shape of the energy distributions for neutrinos and background. The evaluation of possible systematic error arising from these aspects is beyond the scope of this paper.

4.1 Production of reference energy distribution (PDFs)

The energy PDFs used in the fit are obtained from Monte Carlo simulations performed with the official JUNO offline software framework based on Geant4 and customized for the experiment [61]. This code fully describes the detector response, taking into account all the physics processes occurring in the detector: from energy deposition, light emission, propagation and detection, up to the electronics signal processing and event reconstruction algorithms.

The event reconstruction is performed by the official JUNO software code. The analysis energy estimator is the total charge collected by each PMT, expressed as the number of detected photoelectrons (p.e.), subtracted by the mean dark noise hits expected, and including an effective correction to account for the non-uniformity of the detector energy response.

All the neutrino signal and background components have been simulated uniformly within a $r_{\text{sim}} < 15.0 \text{ m}$ sphere, while the fiducial volume employed for this sensitivity analysis is a $r_{\text{FV}} < 14.0 \text{ m}$ sphere.

For each of the species of interest, a PDF of the reconstructed energy variable can be built directly from the corresponding Monte Carlo sample. Because of the huge statistics that will be acquired in JUNO, the number of simulated events is smaller with respect to what is expected for a real dataset. In principle this could bias the fit result, due to statistical fluctuations in the PDFs. We solve this issue by applying an optimized low-pass filter [62] on the generated PDFs, suppressing as much as possible the high-frequency fluctuations without distorting the spectral features.

4.2 Toy dataset generation

The TFC-tagged and TFC-subtracted energy distributions for each toy dataset are obtained by randomly sampling the PDFs of each neutrino and background components. The sampling is Poissonian, assuming the expected number of events as central value. Examples of generated datasets, for six years of data in the different radiopurity scenarios, are shown in Fig. 3, highlighting separately the ${}^7\text{Be}$, pep , ${}^{13}\text{N}$, and ${}^{15}\text{O}$ solar neutrino contributions. The TFC-subtracted and TFC-tagged datasets are shown in the left and right panels, respectively. Note that in the Borexino-like and Ideal scenarios, the signal due to ${}^7\text{Be}$ solar neutrinos (a characteristic Compton-like shoulder at ≈ 1000 p.e.) can be easily seen by eye. On the other hand, in the most pessimistic IBD scenario, the ${}^{238}\text{U}$ and ${}^{232}\text{Th}$ chain decays dominate the count rate in the entire ROI. The contribution of every individual neutrino and background species considered for the sensitivity analysis is shown with lines of different colours, for the baseline scenario in Fig. 4.

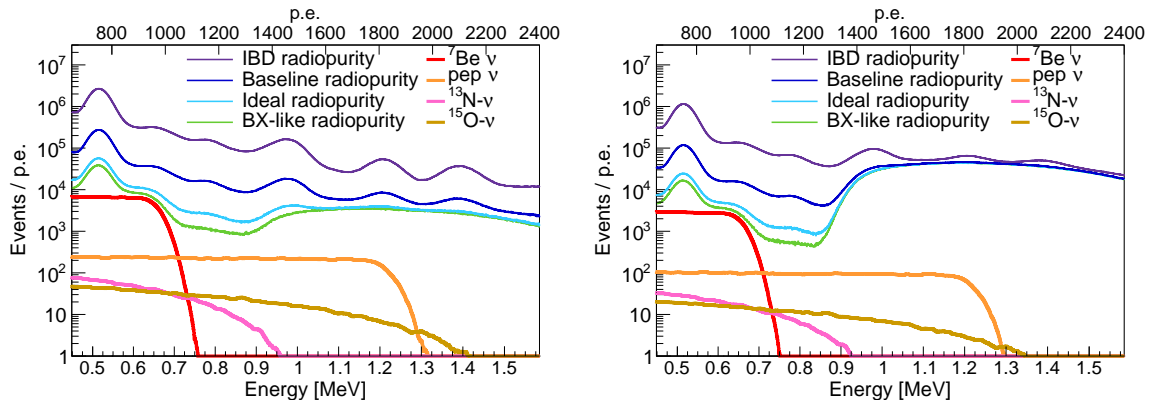


Figure 3. Examples of simulated energy spectra employed for the sensitivity analysis, for six years of data taking. The different solid lines correspond to the four analyzed radiopurity scenarios: IBD (purple line), baseline (blue line), ideal (light blue line), and Borexino-like (green line). The TFC-subtracted and TFC-tagged datasets are reported in the left and right panels. The ${}^7\text{Be}$, pep , ${}^{13}\text{N}$, and ${}^{15}\text{O}$ neutrino contributions are shown as red, orange, pink, and golden tickers solid lines, respectively.

4.3 Multivariate fit

To extract the signal and background contributions from each dataset, the generated TFC-tagged and the TFC-subtracted spectra are fitted simultaneously, minimizing a Poissonian binned likelihood function. This is built as the product of two independent standard Poissonian likelihoods associated to the TFC-tagged and TFC-subtracted spectra. The fit parameters are the numbers of events for each involved signal and background components. Constraints on some of the fit parameters, coming from information which is external and

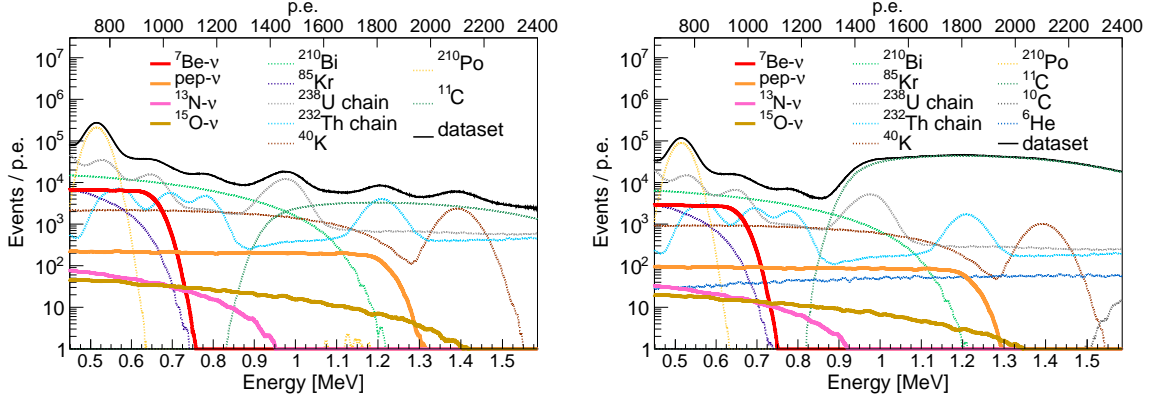


Figure 4. The contributions of all the neutrino and background species considered for the sensitivity analysis for six years of data taking, in the baseline radiopurity scenario. The TFC-subtracted and TFC-tagged datasets are reported in the left and right panels, respectively. The ${}^7\text{Be}$, pep , ${}^{13}\text{N}$, and ${}^{15}\text{O}$ solar neutrino contributions are shown as red, orange, pink, and golden solid lines, respectively. The background contributions (${}^{210}\text{Bi}$, ${}^{210}\text{Po}$, ${}^{85}\text{Kr}$, ${}^{40}\text{K}$, ${}^{238}\text{U}$ chain, ${}^{232}\text{Th}$ chain, ${}^{11}\text{C}$, ${}^{10}\text{C}$, ${}^6\text{He}$) are displayed as dotted lines.

independent from the spectral fit, can be applied in the form of multiplicative Gaussian pull terms to the overall likelihood. The neutrinos and the internal radioactivity (${}^{210}\text{Bi}$ and ${}^{210}\text{Po}$ from the ${}^{210}\text{Pb}$ chain, ${}^{85}\text{Kr}$, ${}^{40}\text{K}$, ${}^{238}\text{U}$ chain, ${}^{232}\text{Th}$ chain) populate the TFC-tagged and TFC-subtracted datasets in the same relative proportions. The long-lived ${}^{11}\text{C}$ isotope instead is present in both datasets, but with two different contributions due to the application of the TFC algorithm. To account for this, two independent fit parameters are included (${}^{11}\text{C}_{\text{sub}}$ and ${}^{11}\text{C}_{\text{tag}}$). The other two most relevant cosmogenic isotopes ${}^{10}\text{C}$ and ${}^6\text{He}$ are included in the TFC-tagged dataset only, given their negligible contribution to the TFC-subtracted dataset [12]. Indeed, the estimated rate for these two isotopes in TFC-subtracted dataset rates are $R({}^{10}\text{C})_{\text{Sub}}^{\text{ROI}} < 0.025 \text{ cpd/kton}$ and $R({}^6\text{He})_{\text{Sub}}^{\text{ROI}} < 1.27 \text{ cpd/kton}$, respectively. We have not included in this analysis the short-lived cosmogenic isotopes since we assume that the veto applied after each muon crossing the detector will be sufficient to effectively remove them (see Sec. 3.3).

The reference energy PDFs used to build the toy datasets are employed as the underlying model distributions for the fit. With this assumption, the Monte Carlo simulations are implicitly supposed to accurately reproduce the detector response. The study of systematic errors associated to the non-perfect knowledge of the detector energy response is beyond the scope of this paper and will not be discussed here.

5 Solar neutrino spectroscopy

Thanks to the large active mass and the unprecedented energy resolution, JUNO will be very competitive in the solar neutrino spectroscopy field. Of course, the achievable precision to ${}^7\text{Be}$, pep , and CNO fluxes is strongly related to the overall exposure and to the signal over background ratio, which in turn depends on the scintillator radiopurity levels. We have performed the sensitivity studies as a function of exposure and for the four different background scenarios described in Sec. 3. For each exposure and background condition a large number (10^4) of toy-datasets is simulated and fitted in order to evaluate the capability of the

multivariate fit to disentangle the signal and background components correctly. The median of the relative statistical error distribution is quoted as the detector sensitivity; the left and right errors are extracted as the distances between the median and the 34% C.L. band extremes. The analysis ROI is $650 \text{ p.e.} < E_{\text{rec}} < 2400 \text{ p.e.}$, corresponding to $0.45 \text{ MeV} < E_{\text{vis}} < 1.6 \text{ MeV}$.

As an example, the correlation plots for a given experimental configuration (baseline radiopurity scenario, six years of data taking) is shown in Fig. 5. In this specific example, all rates are reconstructed without bias, *i.e.* the red histograms are Gaussians centered on the injected values (black vertical lines). The figure outlines also the correlations between different rates in the fit: in particular, the most relevant correlations for the solar neutrino spectroscopy exist between the ^{210}Bi , ^{11}C , CNO, and *pep* rates. While in this particular example these correlations do not influence significantly the performance of the fit, in other scenarios with worst signal to background conditions, they may severely affect it, biasing the results. Whenever this happens, it is necessary to help the fit by imposing external constraints on some of the signal or background rates as will be discussed in the following, especially for what concerns the CNO neutrinos case. It is worth to note that imposing constraints helps the sensitivity even if the reconstructed rates are unbiased.

In most cases, we will show the sensitivity results as a function of data taking time or exposure. Note that, since we employed a spherical FV cut with $r_{\text{FV}} < 14.0 \text{ m}$, 1 year of data taking corresponds to an overall exposure of $\mathcal{E} = 9.87 \text{ kton} \times \text{y}$, and the default TFC performance parameters (see Sec. 3.3) are TP = 0.90 and SE = 0.70.

5.1 Sensitivity on ^7Be neutrinos

The high rate ($\approx 500 \text{ cpd/kton}$) and distinct spectral shape of the ^7Be neutrino signal makes it a relatively easy target for the analysis in JUNO, even in the worse background conditions discussed here (the so-called IBD scenario). We find that for each scenario the ^7Be neutrino rate is extracted with no-bias. Of course, the exposure and background conditions affect the uncertainty with which the rate is reconstructed. This can be clearly seen in upper left plot of Fig. 6, where the relative error of ^7Be on the reconstructed neutrino rate is shown as a function of the data taking time (lower scale) and exposure (upper scale). Borexino-like, ideal, baseline, and IBD radiopurity scenario trends are shown in green, light blue, blue, and purple solid lines, respectively. The best Borexino result on ^7Be neutrinos [12] of 2.7% is reported as a black dotted line. We find that JUNO will be competitive after 1 year of data taking, exceeding the Borexino best result in most of cases. For longer data taking it will reach unprecedented statistical errors, from $\approx 1.0\%$ in the pessimistic IBD scenario to $\approx 0.15\%$ in the BX-like case.

Due to the overlap of their energy spectra, the ^7Be neutrinos precision can be influenced mainly by ^{226}Ra , ^{210}Po , and ^{85}Kr backgrounds levels. The results for increasing contamination level of these backgrounds are reported in upper right panel and in bottom panels of Fig. 6. The bold cross markers correspond to the standard radiopurity scenarios, *i.e.* IBD, Baseline, Ideal, and Borexino-like with no extra background added.

^{226}Ra could be present out-of-equilibrium with respect to the ^{238}U chain due to its chemical differences with its progenitors. For this reason, we have estimated the impact of possible extra-contributions from this isotope. The highest ^{226}Ra contamination selected amounts to ten times the detector design requirement, $c_{\text{Ra}}^{\text{req.}} = 5 \times 10^{-24} \text{ g/g}$, corresponding to 142 cpd/kton overall rate for the $^{226}\text{Ra} \rightarrow ^{206}\text{Pb}$ sub-chain. The results can be found in the upper right plot of Fig. 6. The impact of non-equilibrium contamination of ^{226}Ra in the scintillator, whose concentration is written as c_{Ra} from now on, is assessed by fitting the

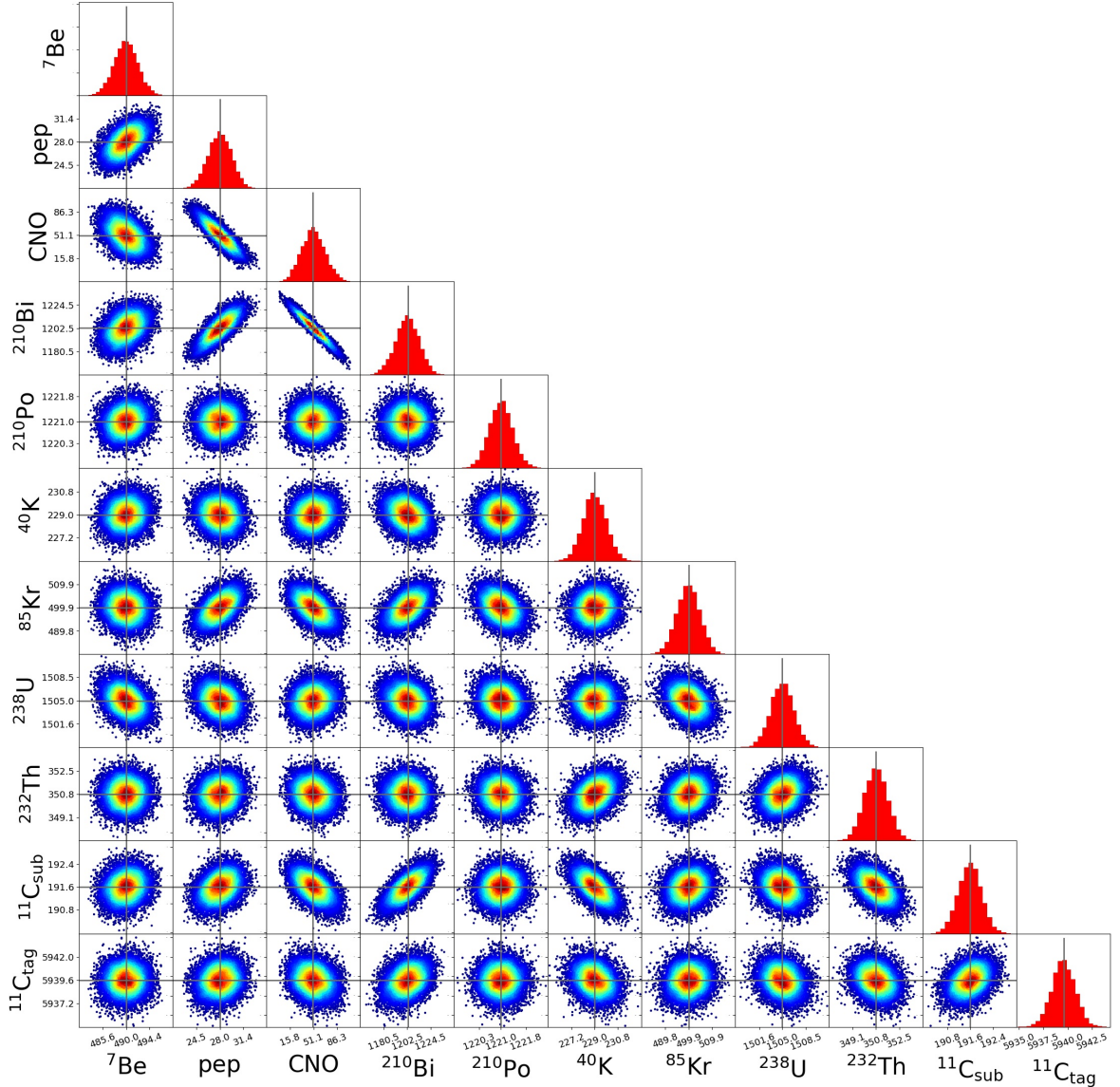


Figure 5. Example correlation plots obtained from the sensitivity study, performing 10^4 fits in the baseline radiopurity scenario for six years of data taking. The red histograms display the distributions of the best-fit reconstructed rates, expressed in cpd/kton units. The non-diagonal frames report the correlation plots among the different species: the rates density increases going from blue to red tones.

sum of all chain contributions from ^{226}Ra down to ^{206}Pb as an additional component. Its presence does not introduce new features in the reconstructed energy spectrum, and its rate determination is also eased by the prominent α decay peaks. At the detector requirement levels, its contribution can be easily identified by the multivariate fit and does not spoil the analysis. Moving from $c_{\text{Ra}} = c_{\text{Ra}}^{\text{req.}}$ to $c_{\text{Ra}} = 5 \times c_{\text{Ra}}^{\text{req.}}$, the ^7Be relative uncertainty only slightly increases (as for example, going from $\approx 0.4\%$ to $\approx 0.5\%$ in BX-like scenario, and from $\approx 0.45\%$ to $\approx 0.55\%$ in Ideal scenario). For the highest c_{Ra} injected in the case of baseline and IBD scenarios, the reconstructed ^7Be rate is biased, therefore we do not report the related points on the plot.

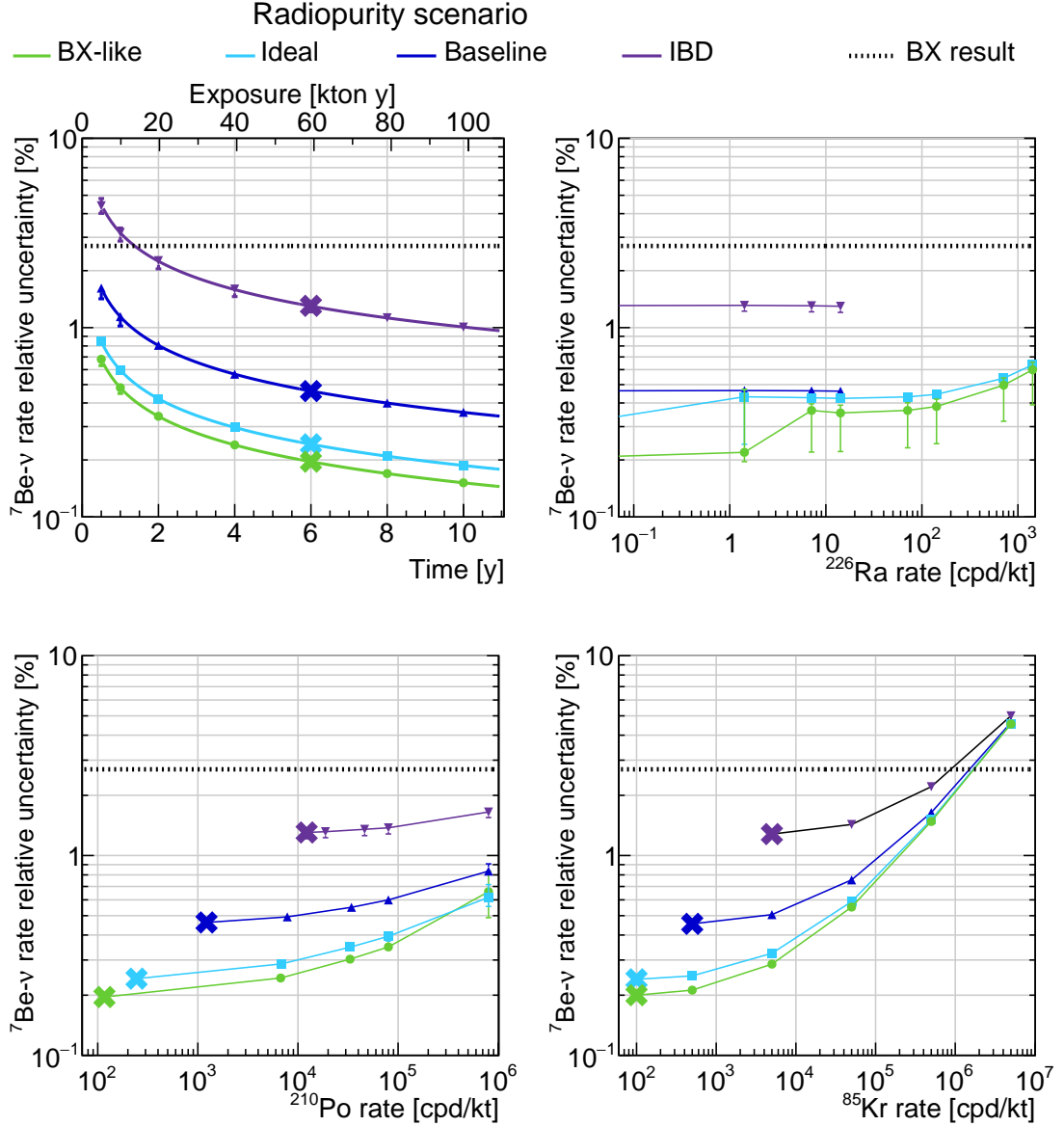


Figure 6. Upper left panel: the relative uncertainties of ${}^7\text{Be}$ neutrino rates as a function of exposure. Borexino-like, ideal, baseline, and IBD radiopurity scenario trends are shown respectively in green, light blue, blue, and purple solid lines. The best Borexino result (2.7%) [12] is indicated by the black dotted line. Upper right, bottom left, and bottom right panels: the relative uncertainty of ${}^7\text{Be}$ neutrino rates as a function of the rate of ${}^{226}\text{Ra}$ chain, ${}^{210}\text{Po}$ (expressed as the sum for ${}^{210}\text{Po}$ from ${}^{210}\text{Pb}$ and out of equilibrium one), and ${}^{85}\text{Kr}$ respectively, for 6 years of data taking. The bold cross markers correspond to the standard radiopurity scenarios for 6 years of data taking, i.e. IBD, baseline, ideal, and Borexino-like with no extra background added. For what concerns the upper left plot, the standard radiopurity scenarios have no extra-contaminations of ${}^{226}\text{Ra}$, therefore no cross is shown.

A potentially dangerous isotope for the ${}^7\text{Be}$ analysis is the unsupported ${}^{210}\text{Po}$, that decays to stable ${}^{206}\text{Pb}$. In fact, it is possible that a certain amount of ${}^{210}\text{Po}$ will be present out-of-secular-equilibrium with respect to ${}^{238}\text{U}$ and ${}^{210}\text{Pb}$ decay chains, as experienced both by Borexino and KamLAND immediately after filling [52, 53]. To study the impact of this

isotope on the JUNO sensitivity to ${}^7\text{Be}$ solar neutrinos, we have simulated for each standard scenario an extra contribution of ${}^{210}\text{Po}$ up to $8 \times 10^5 \text{ cpd/kton}$. The results can be found in the lower left plot of Fig. 6. From this plot the effect of this isotope on ${}^7\text{Be}$ neutrinos is evident. However, even if JUNO started out with a ${}^{210}\text{Po}$ contamination of the order of the one experienced at the beginning of Borexino (about $8 \times 10^4 \text{ cpd/kton}$), the ${}^7\text{Be}$ neutrino rate would still be determined with an uncertainty of $\approx 1.4\%$ (IBD), $\approx 0.6\%$ (baseline), $\approx 0.4\%$ (Ideal), and $\approx 0.35\%$ (Borexino-like). Even in the most pessimistic scenario, JUNO will be still able to improve the best 2.7% Borexino result on ${}^7\text{Be}$ rate.

Finally, one of the most important backgrounds for the ${}^7\text{Be}$ solar neutrino analysis is ${}^{85}\text{Kr}$, since the two spectra almost overlap. The ${}^{85}\text{Kr}$ contamination level is difficult to predict and could be potentially high for a number of reasons: for example, air-leak during filling or emanation from the acrylic vessel (${}^{85}\text{Kr}$ could be adsorbed by the acrylic surface due to exposure to air during construction). To study the impact of a large contamination of ${}^{85}\text{Kr}$, we have simulated for each scenario an extra contribution of ${}^{85}\text{Kr}$ up to a value of $5 \times 10^6 \text{ cpd/kton}$ in addition to the ${}^{85}\text{Kr}$ included in each scenario. The results are shown in lower right plot of Fig. 6, where one can clearly see how the uncertainty gets worse for all scenarios. Nevertheless, when the ${}^{85}\text{Kr}$ rate is kept below about $1 \times 10^6 \text{ cpd/kton}$, the ${}^7\text{Be}$ statistical error is still lower than the 2.7% best result from Borexino.

5.2 Sensitivity on *pep* neutrinos

The *pep* neutrino flux is relatively low, approximately fifty times smaller than the ${}^7\text{Be}$ neutrino one. The current theoretical and experimental information, including the solar luminosity constraint [63], the ratio of *pp* to *pep* neutrino rate, the global fit of solar neutrino data [64], and the oscillation parameters [65], allows to determine the *pep* neutrino flux at 1.4% level. To experimentally verify these assumptions, it is important to measure directly the *pep* neutrino flux, which has been determined previously by Borexino with 17% precision [12]. Moreover, this result was obtained by fixing the CNO rate to the SSM prediction; in the following, it will be shown how JUNO will be able to measure the *pep* neutrino flux without this constraint for the first time.

The analysis is complicated by the poor signal to noise ratio: the most annoying backgrounds, existing in the same energy region of *pep* neutrinos, are the radioactive decays of ${}^{210}\text{Bi}$ and of the cosmogenic isotope ${}^{11}\text{C}$. Furthermore, the *pep* neutrino signal has a comparable rate and a similar energy distribution to the one of CNO neutrinos, which induces strong correlations in the fit between the two, as shown in Fig. 5. The results for the relative uncertainties on the *pep* rate, in the four radiopurity scenarios, are shown in Fig. 7, as a function of the data taking time (lower scale) and exposure (upper scale). For comparison, the best Borexino result (17%) [12] is highlighted as a black dashed line. In all scenarios the fit is able to reconstruct with no-bias the injected *pep* rate after one year of data taking, except for the worst radiopurity scenario, IBD, where a longer time of six years is needed.

We find that after 6 years of data taking, JUNO will reach competitive statistical uncertainties matching or exceeding the Borexino best result in all radiopurity scenarios: $\approx 17\%$ (IBD), $\approx 6.7\%$ (baseline), $\approx 3.9\%$ (ideal), and $\approx 3.1\%$ (Borexino-like). After ten years, the statistical uncertainties reaches unprecedented values: $\approx 13\%$ (IBD) $\approx 5.1\%$ (baseline), $\approx 3.0\%$ (ideal), and $\approx 2.4\%$ (Borexino-like).

Since ${}^{11}\text{C}$ is one of the most relevant backgrounds for the *pep* analysis, we performed a dedicated study to understand the impact of the TFC performance on the sensitivity. In Fig. 8, we show the statistical uncertainty (color scale) as a function of the TFC parameters SE

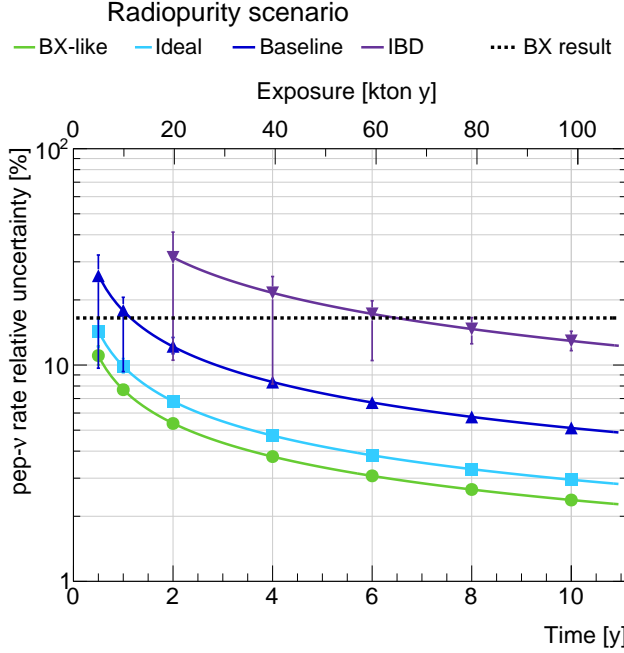


Figure 7. The relative uncertainties of *pep* neutrino rate as a function of exposure. Borexino-like, ideal, baseline, and IBD radiopurity scenario trends are shown respectively in green, light blue, blue, and purple solid lines. The best Borexino result (17%) [12] is indicated by the black dotted line.

(Subtracted Exposure) and TP (Tagging Power) for the ideal and IBD radiopurity scenarios (left and right panel, respectively). For the Borexino-like scenario, the *pep* neutrino precision is notably affected by the TFC performances. Particularly, the TP parameter plays a central role with respect to SE, suggesting how the capability to efficiently identifying the ^{11}C is more relevant than having a high fraction of exposure included in the TFC-Subtracted spectrum. Indeed, the *pep* rate precision is almost doubled scanning the analyzed TP range even for constant SE. The same conclusions can be drawn for the ideal and baseline scans. Instead, the IBD scenario implies high levels of ^{238}U and ^{232}Th chains isotopes, such that their spectra dominate the *pep* energy region. As a consequence, even an excellent ^{11}C discrimination performance do not increase significantly the signal over background ratio and therefore do not significantly improve the precision of the measurement of the *pep* neutrinos. A comprehensive overview of the impact of TP on *pep* precision for the four radiopurity scenarios can be found in Fig. 9.

5.3 Sensitivity on CNO neutrinos

As experienced by Borexino [13, 14], the search for CNO neutrinos has two main obstacles: the low signal rate and the presence of several backgrounds existing on the same energy window, *i.e.* *pep* neutrinos, ^{11}C , and ^{210}Bi . For what concerns the ^{11}C events, they can be efficiently identified by the TFC algorithm, as described in Sec. 3.3.1: the impact of the TFC performance on the CNO sensitivity will be addressed later in this Section. On the other hand, the main problem is represented by the CNO spectral shape degeneracy with the *pep* neutrinos and the ^{210}Bi background.

The results on the sensitivity are shown in left panel of Fig. 10, where the relative uncertainties on the CNO rate in different radiopurity scenarios are plotted as a function of

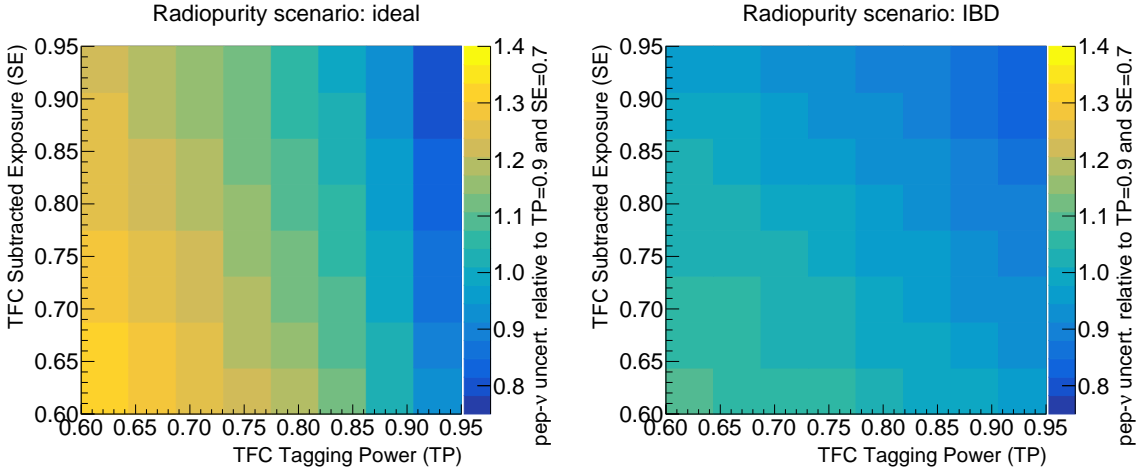


Figure 8. Impact of TFC performance on *pep* neutrino results: the *pep* neutrino rates relative uncertainty (color scale) is shown as a function of Tagging Power (*x*-axis) and Subtracted Exposure (*y*-axis), after 6 years of data taking. The *z*-axis (color scale) represents the *pep* neutrino uncertainties relative to *pep* uncertainty when $TP = 0.9$ and $SE = 0.7$. The rate uncertainty increases going from blue to yellow tones. Ideal and IBD scenarios are shown in left and right panels, respectively.

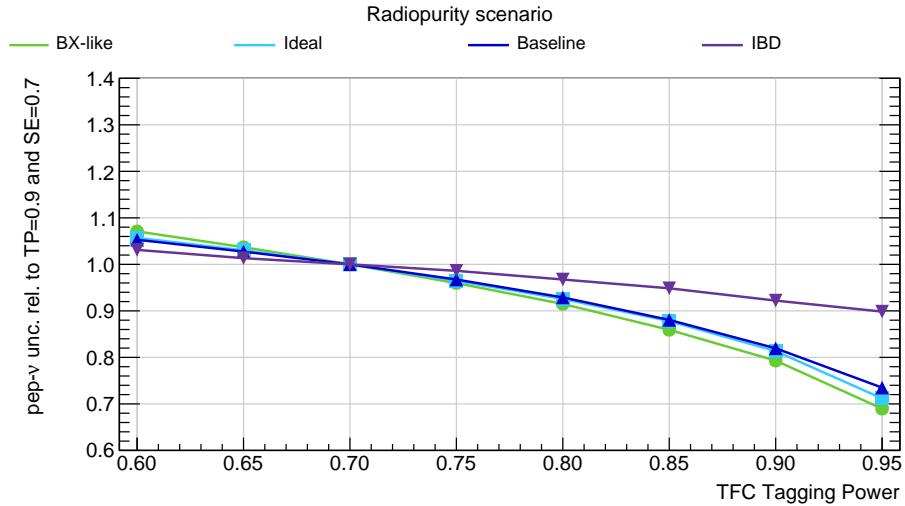


Figure 9. Impact of TFC performance on *pep* neutrino results: the *pep* neutrino rates relative uncertainty, normalized by the one obtained when $TP = 0.9$ and $SE = 0.7$ as a function of the TFC Tagging Power, is shown for a fixed $SE = 0.7$ value. Borexino-like, ideal, baseline, and IBD radiopurity scenario trends are shown respectively in green, light blue, blue, and purple solid lines.

data taking time (lower scale) and exposure (upper scale).

As expected, the sensitivity to CNO neutrinos is strongly dependent on the radiopurity scenario assumed. In the Borexino-like and ideal scenarios after two years of data taking, JUNO will reach a CNO relative error of $\approx 30\%$ and $\approx 39\%$, respectively, being thus comparable with the precision achieved by Borexino [14]. The situation is more critical in the baseline scenario: in this case, the output of the fit for the CNO rate is affected by a bias unless we wait for several years (> 6 years). In the IBD scenario, the fit produces biased

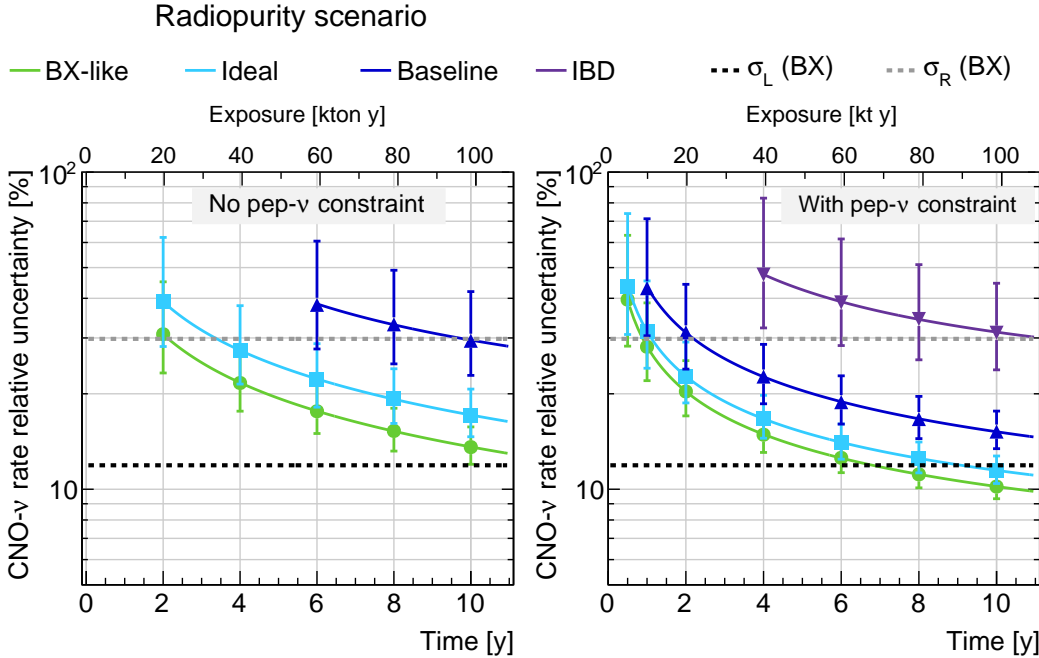


Figure 10. Relative uncertainty of the CNO rate as a function of exposure and time without and with a constraint on the *pep* neutrino rate (left and right panels, respectively). Borexino-like, ideal, baseline, and IBD radiopurity scenario trends are shown respectively in green, light blue, blue, and purple solid lines. The Borexino results are reported as a black and grey dotted horizontal lines (corresponding to the left σ_L and right σ_R uncertainties [14]). Note that the Borexino results have been obtained constraining the *pep* neutrino rate and putting an upper limit on the ^{210}Bi rate. As discussed in the text, the fit produces biased results on CNO rate for IBD scenario without *pep* rate, even after many years of data taking; for this reason, these results are not shown in the plot.

results on CNO rate, even after many years of data taking; for this reason, it is not shown in the plot.

In order to reduce correlations, we constrain the *pep* neutrino interaction at 1.4% as discussed in Sec. 5.2. Following this approach, the CNO sensitivity greatly improves, as can be seen in the right panel of Fig. 10: for data taking period longer than 6 years, the relative uncertainty reduces to the level of $\approx 10\%$, $\approx 12\%$, and $\approx 15\%$ for Borexino-like, ideal, and baseline scenarios, respectively. This result would be precise enough to pave the way to a direct measurement of the solar metallicity using solar neutrinos. As previously mentioned, this study takes into account the statistical error only. At this level, the measurement will be largely dominated by systematic errors, which therefore must be under control to maintain a competitive sensitivity. On the other side, even in the IBD radiopurity scenario the CNO neutrino rate can be measured at 31% level after 10 years of data taking.

The contribution of potentially problematic additional sources of backgrounds, such as ^{210}Po , ^{85}Kr , and pileup, were found to be negligible and will not be discussed in detail.

As discussed in Sec. 5.2 for the *pep* measurement, the precision on CNO neutrino rate is expected to be strongly dependent on the TFC performance. We performed the TFC studies considering the fit configuration, where all the species have been left free to vary, assuming all the radiopurity scenarios, except the IBD one since in this case we have limited sensitivity to CNO neutrinos, as discussed above. The results as a function of TP and SE are shown

in Fig. 11 for the ideal radiopurity scenario. The color scale represents the CNO neutrino uncertainties relative to the values obtained when $TP = 0.9$ and $SE = 0.7$ (the default values). Similarly to what was obtained in Sec. 5.2, the tagging power is more relevant than the subtracted exposure in increasing the ability of the fit to identify CNO neutrinos. For the other radiopurity scenarios, we achieve the same conclusions as for the *pep* neutrinos.

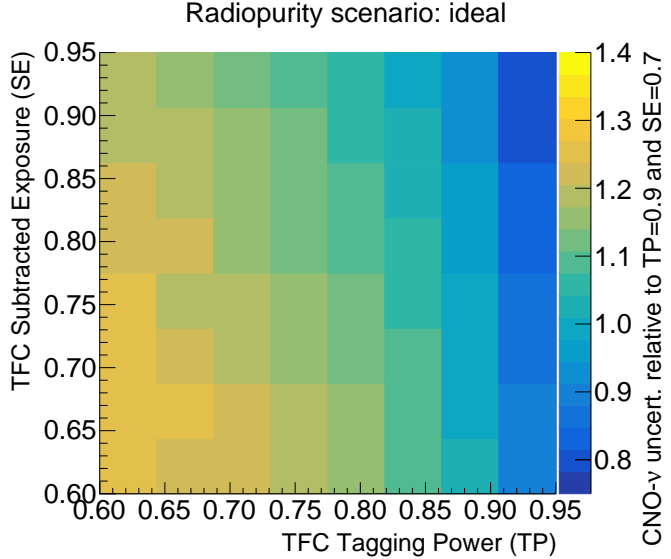


Figure 11. Impact of TFC performance on CNO neutrino results: the CNO neutrino rates relative uncertainties (color scale) is shown as a function of Tagging Power (x -axis) and Subtracted Exposure (y -axis), after 6 years of data taking in the ideal radiopurity scenario. The z -axis (color scale) represents the CNO neutrinos uncertainties relative to CNO uncertainty when $TP = 0.9$ and $SE = 0.7$.

5.4 Sensitivity results on ^{13}N and ^{15}O neutrinos

The CNO solar neutrinos come mainly from two reactions, the $^{15}\text{O} \rightarrow ^{15}\text{N} + e^+ + \nu_e$ (producing the so-called ^{15}O neutrinos) and the $^{13}\text{N} \rightarrow ^{13}\text{C} + e^+ + \nu_e$ (producing the so-called ^{13}N neutrinos). In the previous paragraph, the spectral distribution of electrons scattered by CNO neutrinos has been used in the fit as a whole, keeping the contributions from ^{13}N and ^{15}O neutrinos fixed to the SSM value, which are 47.6% and 52.4%, respectively. The sub-dominant ^{17}F neutrinos have a degenerate energy spectrum with ^{15}O . These numbers take into account the electron-scattering cross section: indeed, at production the relative proportion of ^{13}N and ^{15}O is 57% and 43% respectively, but ^{15}O neutrinos have a slightly higher probability of interacting in JUNO since their energy distribution extends to higher values. Thanks to the large exposure and high energy resolution, JUNO might be able to extract individually the rates of ^{13}N and ^{15}O neutrinos from the fit. Note that a separate measurement of these neutrino fluxes – never achieved by any experiment so far – would be an important step forward towards understanding the metallicity of the solar core.

The ^{13}N and ^{15}O sensitivity studies were performed both with all the species free to vary in the fit and, secondly, constraining the *pep* neutrino rate as it was done for the full CNO analysis (see Section 5.3). The results for both ^{13}N and ^{15}O neutrinos are shown in the left and right panel of Fig. 12, respectively. The solid lines refer to the configuration with all

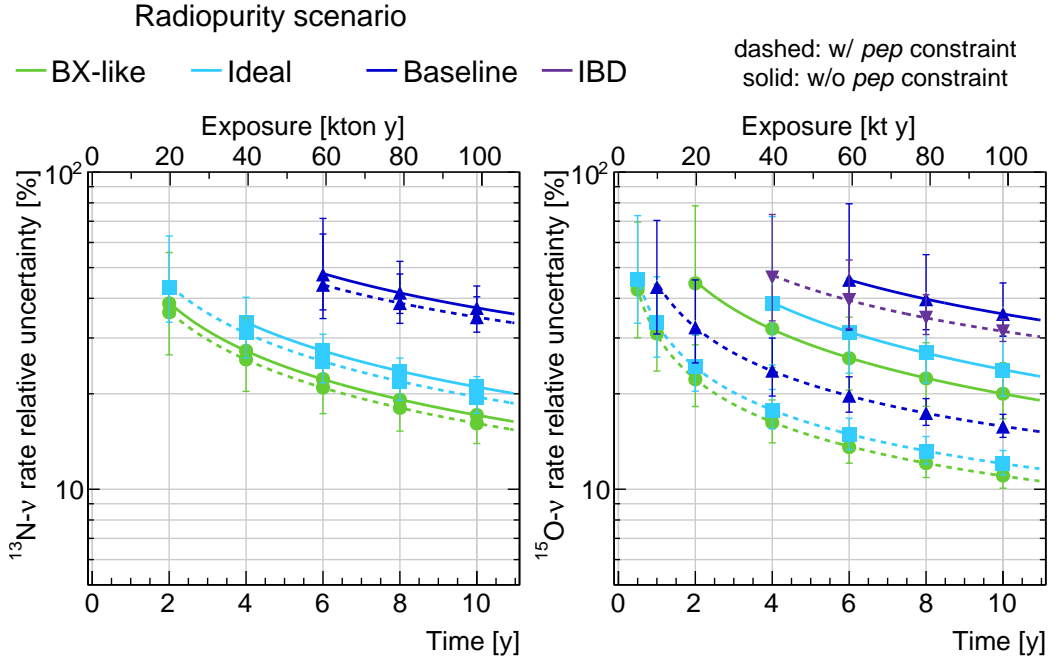


Figure 12. The relative uncertainty of ^{13}N (left panel) and ^{15}O (right panel) neutrino rates as a function of exposure. Borexino-like, ideal, baseline, and IBD radiopurity scenario trends are shown respectively in green, light blue, blue, and purple lines. The solid lines refer to the fit configurations where all the species have been left free to vary, while the dashed lines to the configuration where the rate of *pep* neutrinos has been constrained.

species free in the fit, while the dotted ones correspond to the case where a *pep* constraint was imposed.

If no *pep* constraint is applied, considering a 10 years data taking, in the IBD scenario JUNO will not be sensitive to either neutrino species and therefore we do not show any result, while in the baseline scenario ^{13}N and ^{15}O relative errors will reach 37% and 36%, respectively. Instead, in the two most radiopure scenarios JUNO will have the potential to measure ^{13}N neutrinos with a precision of $\approx 21\%$ (Ideal) and $\approx 17\%$ (BX-like), and ^{15}O neutrinos with a $\approx 24\%$ (Ideal) and $\approx 20\%$ (BX-like) relative error. Note that, in general, ^{15}O neutrinos are determined with a larger error than ^{13}N neutrinos, because their spectral shape and endpoint are similar to the ones of *pep* neutrinos. For this reason, the introduction of a constraint on the *pep* neutrino rate affects mostly the results on ^{15}O neutrinos which improve significantly, while the ^{13}N ones are only marginally affected. In particular, after 10 years the ^{15}O neutrino relative errors reduce to the values of $\approx 16\%$ (Baseline), $\approx 12\%$ (Ideal), and $\approx 11\%$ (BX-like). Furthermore, ^{15}O neutrinos can now be detected even in the IBD case, with a relative error of 32%.

6 Periodic modulations of the ^7Be neutrino rate

In this Section we will discuss the JUNO potential to measure time variations of the solar neutrino fluxes. In particular, we will focus on ^7Be solar neutrinos which are by far the dominant component in the energy range discussed in this paper.

One obvious time variation of the solar neutrino flux is the seasonal modulation induced by the eccentricity of the Earth’s orbit around the Sun. Since this effect is well-established and known with high precision [19, 66], it will not be further investigated here.

Solar neutrinos travelling at night towards terrestrial detectors cover some distance inside the Earth so that their oscillations are affected by the Earth’s matter, responsible for coherent re-generation of the electron flavor eigenstate. This fact leads to a difference between the day and night solar neutrino signal ΔR , the so-called *day-night modulation*, which magnitude depends on both the neutrino energy and the oscillation parameters [67]. In the MSW-LMA neutrino oscillation scenario the expected asymmetry for the energies of ${}^7\text{Be}$ neutrinos interacting via elastic scattering is small, $A_{\text{DN}} = \Delta R / \langle R \rangle \lesssim 0.1\%$ [68] where $\langle R \rangle$ is the average of day and night rates. However, some theories involving non-standard interactions of solar neutrinos open the possibility for larger *day-night modulations* [69–72]. So far, no experiment has reached enough sensitivity to see the low level of asymmetry predicted in the MSW-LMA frame at the ${}^7\text{Be}$ neutrino energies. The best result has been obtained by Borexino, which finds no asymmetry within a $\approx 1\%$ error [22, 66].

A third physical source for modulations could be the temperature variations in the solar core induced by gravity-driven (g-modes) helioseismic waves. Since solar neutrino production rates highly depend on temperature via $\phi \propto T^\alpha$ (with $\alpha=11$ for ${}^7\text{Be}$ neutrinos [73]) even small temperature change may give raise to modulations of the solar flux with periods in the range between several hours and minutes [74–76].

In the following, we investigate the JUNO capability to detect the day-night and the gravity-driven modulations of ${}^7\text{Be}$ solar neutrino rate.

6.1 Sensitivity to solar neutrino day-night asymmetry

We have investigated the sensitivity of JUNO to day-night modulations in two complementary ways: the *statistical subtraction* and the *Lomb Scargle* (LS) methods.

6.1.1 The statistical subtraction method

The statistical subtraction method consists in dividing the dataset in two parts - the day and the night one - and determine the asymmetry (or its absence) by searching for a residual ${}^7\text{Be}$ signal in the subtracted spectrum (night minus day). This method has the advantage of cancelling possible long time-scale variations of the backgrounds, but it can be applied only when the period of the modulation is known *a priori*. Indeed, it couldn’t be used for the g-mode modulations described in the next section.

We produced toy datasets with different exposure and background conditions in the same way described in Section 4. For each dataset, we create the Day and Night histograms assuming that all species rates are the same during the day and the night, except for the ${}^7\text{Be}$ neutrinos which are injected with an asymmetry A_{DN} such that:

$$A_{\text{DN}} = \frac{\Delta R}{\langle R \rangle} = 2 \frac{R_{\text{Be}}^N - R_{\text{Be}}^D}{R_{\text{Be}}^N + R_{\text{Be}}^D} \implies R_{\text{Be}}^N = \frac{2 + A_{\text{DN}}}{2 - A_{\text{DN}}} R_{\text{Be}}^D. \quad (6.1)$$

We recall that due to the regeneration of ν_e in Earth, we expect a higher rate of neutrinos at night with respect to day. For each toy dataset we subtract the Day histogram from the Night one, creating in such a way the Difference dataset.

We performed a frequentist hypothesis test by using

$$\Delta\chi^2 = \chi^2_{\text{null}} - \chi^2_{\text{altern}} = \chi^2_{\Delta R=0} - \chi^2_{\Delta R \text{ free}} \quad (6.2)$$

as the test statistics. On one hand, the *null hypothesis* implies that modulations are absent and therefore the ${}^7\text{Be}$ rate of the Difference dataset is assumed to be zero. On the other hand, according to the *alternative hypothesis*, we fit the Difference dataset treating the ${}^7\text{Be}$ rate as a parameter left free to vary. The optimized analysis ROI is $640 \text{ p.e.} < E_{\text{rec}} < 1200 \text{ p.e.}$, corresponding to $450 \text{ keV} < E_{\text{vis}} < 810 \text{ keV}$. An example of the Difference energy spectrum is shown in Fig. 13 for an exposure of 6 years and $A_{\text{DN}} = 0.6\%$, and in the Ideal radiopurity scenario. The resulting ${}^7\text{Be}$ profiles assuming the null hypothesis and the alternative hypothesis are displayed as red dashed or red solid lines respectively.

The sensitivity is evaluated by comparing the $\Delta\chi^2$ distribution obtained in this way and the one obtained with the same procedure when no asymmetry is injected. These distributions are shown respectively as the blue and orange histograms in left plot of Fig. 14. The median sensitivity to reject the null hypothesis (discovery significance) is calculated as the percentage of events of the orange distribution which falls above the median of the blue distribution.

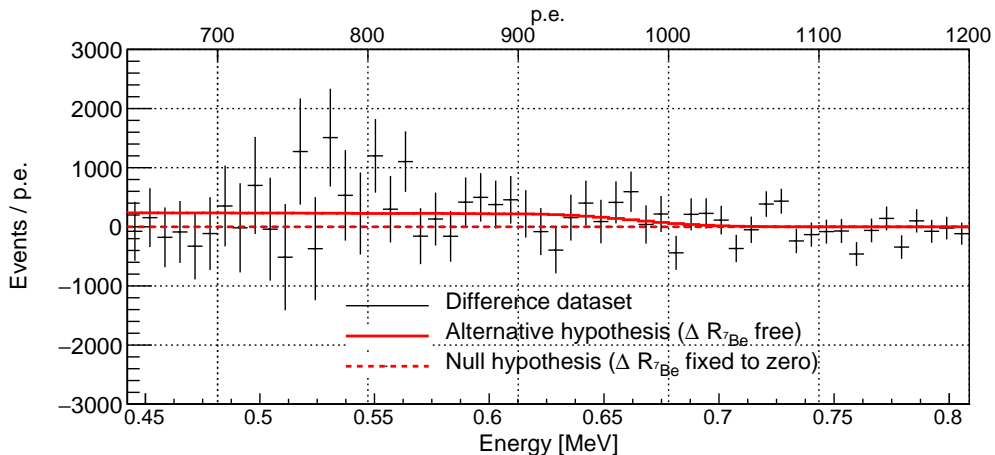


Figure 13. Statistical Subtraction method: difference between the Night and Day datasets when an asymmetry $A_{\text{DN}} = 0.6\%$ is injected (Eq. 6.1), for 6 years of data-taking, in the Ideal radiopurity scenario. The resulting ${}^7\text{Be}$ profiles assuming the null hypothesis and the alternative hypothesis are displayed as red dashed and red solid lines, respectively.

6.1.2 The Lomb Scargle Method

The Lomb Scargle Method is a powerful tool to search for periodic variation in a time series of data [77, 78]. It is an extension of the Fourier Transform to treat datasets which are not evenly distributed in time and has been successfully adopted in several neutrino experiments [17, 19, 79].

Thousands of toy datasets are built for a given day-night asymmetry A_{DN} and a given exposure in the same way as for the statistical subtraction method. The ROI is optimized and constrained to the energy region where ${}^7\text{Be}$ neutrinos are dominant, that is $640 \text{ p.e.} < E_{\text{rec}} < 1040 \text{ p.e.}$, corresponding to $450 \text{ keV} < E_{\text{vis}} < 705 \text{ keV}$. Note that in this case the ROI is narrower than the one used in the statistical subtraction method, because the LS is more sensitive to backgrounds. Data are divided in 1 hour long bins: the bin time width has been

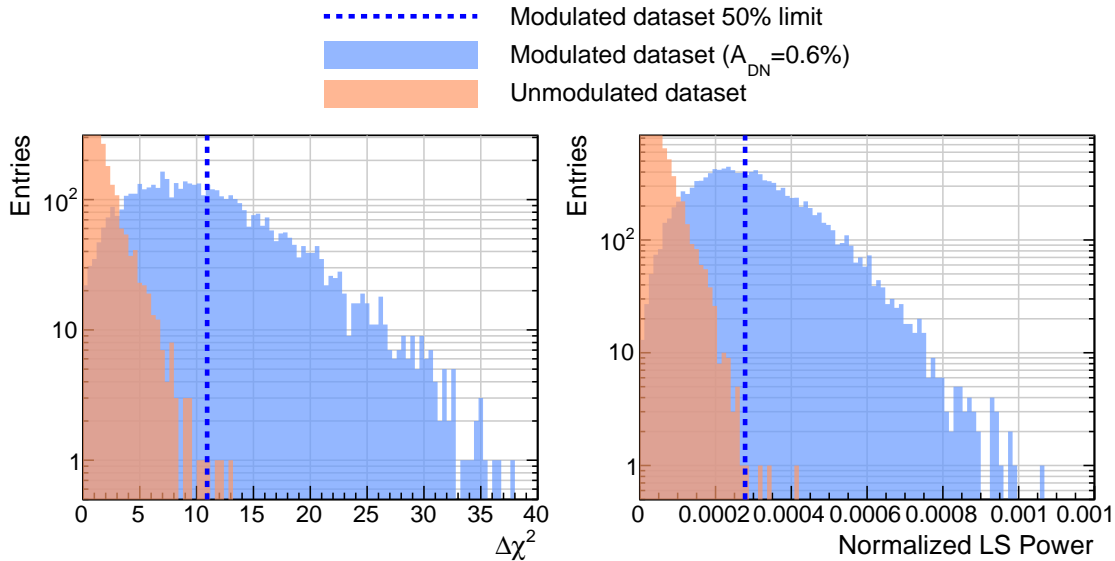


Figure 14. Test statistics distributions for the Statistical Subtraction Method (left) and the Lomb Scargle Method (right). The distributions are obtained from thousands of datasets, where a day-night asymmetry is injected (blue) and when no-asymmetry is injected (orange). In this example, $A_{DN} = 0.6\%$, the radiopurity scenario is the ideal one, and the exposure is 6 years. For more details on how the test statistics is built for each one of the two methods, see text. The median value of the blue curve is shown as a vertical dashed blue line.

optimized to contain enough statistics (about 50 ${}^7\text{Be}$ neutrino events). For each toy dataset, the Lomb Scargle periodogram is created: it represents the spectral density histogram of a signal as a function of frequency. A test statistics function \mathcal{P} , namely the normalized LS power, is built by calculating the difference between the χ^2 , obtained when the periodogram is fitted either with a flat line (χ_0^2) or with a peak at $f = 1/T = 1 \text{ day}^{-1}$ ($\chi_{DN}^2(f)$). This difference is then normalized to χ_0^2 :

$$\mathcal{P}(f) = \frac{\chi_{DN}^2(f) - \chi_0^2}{\chi_0^2}. \quad (6.3)$$

The distribution of normalized LS power for thousands of toy datasets simulated by injecting a given asymmetry A_{DN} , together with the one obtained when no asymmetry is injected, are plotted as blue and orange histograms of Fig. 14. In this particular example, $A_{DN} = 0.6\%$.

As in the statistical subtraction method, the median sensitivity to reject the null hypothesis is given by the percentage of events of the orange distribution falling above the median of the blue histogram.

6.1.3 Results

We performed the sensitivity study for different values of A_{DN} starting from 0.1% (the value expected in the MSW-LMA scenario for the ${}^7\text{Be}$ energies) up to a few %. Following the analysis procedures described above we have studied the minimum day-night asymmetry which could be detected at 3σ by JUNO as a function of exposure and for different radiopurity scenarios. The results are shown in Fig. 15 both for the statistical subtraction and the Lomb

Scargle methods. It is clear that even in the most radiopure scenarios JUNO will not be able to reach the sensitivity to detect with a 3σ significance the A_{DN} predicted by the MSW-LMA effect. However, it will probe unprecedented A_{DN} values: for example, after 10 years, JUNO will be able to discover A_{DN} of the order of 0.3%–0.4% in the two most favourable radiopurity scenarios analyzed. Note that the only experimental result on ADN in the ^{7}Be energy range is the one from Borexino, which finds an asymmetry compatible with zero and only quotes the precision of its measurement (0.94%). This is not directly comparable with the JUNO discovery potential discussed here. The precision estimated for JUNO in the two most favourable radiopurity scenarios after 10 years of data-taking are in the range of 0.1–0.2%, therefore, significantly better than the one achieved by Borexino [22].

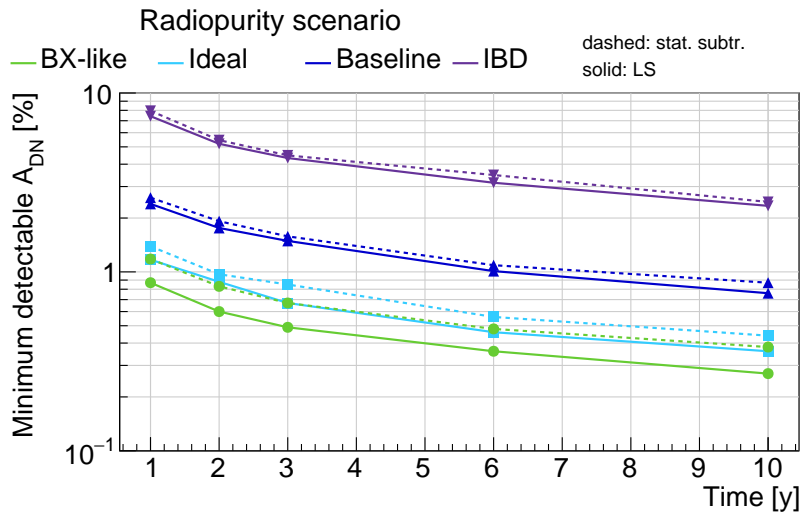


Figure 15. Minimum A_{DN} detectable at 3σ by JUNO as a function of the exposure for the statistical subtraction (dashed) and the Lomb Scargle (solid) methods. Borexino-like, ideal, baseline, and IBD radiopurity scenario trends are shown respectively in green, light blue, blue, and purple lines.

6.2 Sensitivity to g-modes

Following the same procedure described in the previous paragraph, we applied the Lomb-Scargle method also to determine the JUNO sensitivity to g-modes induced asymmetry $A_{g\text{Mode}}$. Since in this case the modulation period T is not known a-priori, we studied the dependence of the sensitivity on T varying from hours to several hundreds days, for different exposures. The outcome of this study can be found in Fig. 16 for an exposure of 10 years, but the results are similar also for shorter exposures. We find that the sensitivity does not significantly depend on T . This means that the results shown in Fig. 15 for the day-night asymmetry studies ($T = 1$ day) are valid also for shorter period modulations due to g-modes. The current best limit for g-mode induced modulations has been set by the SNO experiment (for the ^{8}B solar neutrino energy range) and is 10% [75]. For all radiopurity scenarios considered in this paper, JUNO will be able to improve this limit significantly after a few years of data-taking. In particular, this study shows that after 10 years of data-taking JUNO will have the capability to reveal $A_{g\text{Mode}}$ values as low as 2.5% (IBD scenario), 0.8% (baseline scenario), 0.4% (ideal scenario), and 0.3% (BX-like scenario). This means that the underly-

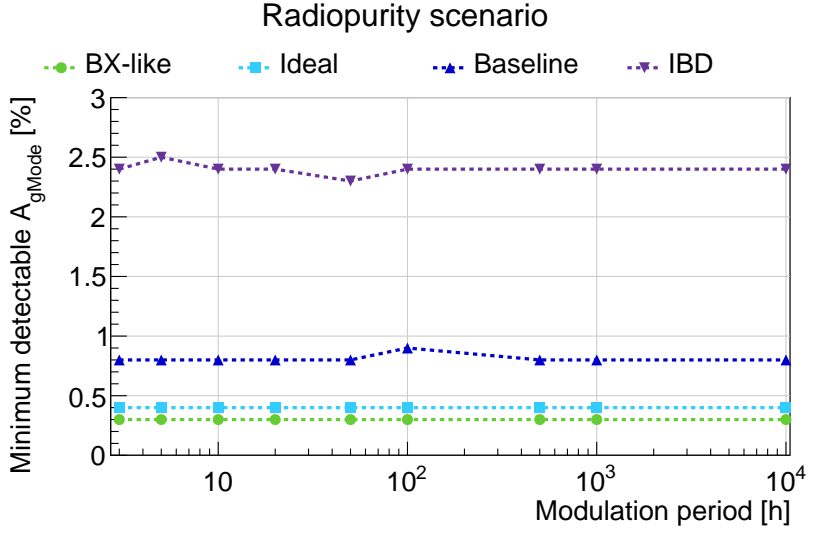


Figure 16. Minimum periodic modulation $A_{g\text{Mode}}$ detectable at 3σ by JUNO as a function of the period T for the four radiopurity scenarios and for 10 years of data-taking. Borexino-like, ideal, baseline, and IBD radiopurity scenario trends are shown respectively in green, light blue, blue, and purple lines.

ing relative temperature fluctuations can be detected down to $\Delta\mathcal{T}/\mathcal{T} \simeq A_{g\text{Mode}}/\alpha \simeq 5 \times 10^{-4}$ (where $\alpha = 11$ is the temperature exponent for ${}^7\text{Be}$ neutrinos). We recall that in this analysis we have included only statistical errors: some systematic errors could for example arise from unexpected time variations of the backgrounds. However, the experience of other experiments, such as Borexino [19, 66], shows that the Lomb Scargle method is a powerful tool to filter away time-varying background and therefore we expect that the addition of this kind of systematic error will not alter significantly the results discussed here.

7 Conclusions

Even decades after their first observation, solar neutrinos represent a prolific field in particle and astro-particle physics. In this paper we have studied the JUNO sensitivity to the so-called *intermediate energy solar neutrinos*: ${}^7\text{Be}$, *pep*, and CNO neutrinos.

We performed the study assuming different radiopurity scenarios and we find that JUNO will be able to measure solar neutrino rates with an uncertainty highly competitive with respect to the current state-of-the-art in the solar neutrino field. In particular, we find that in all the radiopurity scenarios considered the expected uncertainty on ${}^7\text{Be}$ and *pep* will significantly be improved with respect to the Borexino one after a few years of data taking, provided that the systematic error will be kept under control. After six years of data taking, for ${}^7\text{Be}$ neutrinos we will reach the percent level in all the radiopurity scenarios, while for *pep* neutrinos the uncertainty will go from 3% up to 17% depending on the radiopurity scenario. For what concern CNO neutrinos, the results will be highly dependent on the types of backgrounds and their levels. For most radiopurity scenarios (except for the worst one considered) JUNO will be able to reduce the Borexino uncertainty, provided a constraint on the *pep* neutrino rate is set: after 6 years of data taking, the uncertainty on CNO neutrinos will reach a precision ranging from 12% to 19% depending on the radiopurity scenario. Note

that unlike Borexino, this result could be reached without also imposing a constraint on the ^{210}Bi rate. Furthermore, JUNO has the potential to measure individually for the first time the rate of the two main components of the CNO flux, ^{13}N and ^{16}O solar neutrinos, except in case of the worst radiopurity scenario.

In addition, JUNO will be able to study possible periodic modulations of the solar neutrino signal, down to unprecedented levels. In particular, for what concerns the Day/Night asymmetry, it will be able to improve the limit of $\sim 1\%$ obtained by Borexino in all radiopurity scenarios except for the worst one considered. For what concerns the g-mode induced modulation, JUNO will improve the current best limits by one order of magnitude, reaching the percent level in most radiopurity scenarios.

In conclusion, JUNO will play a decisive role in solar neutrino physics, significantly reducing the uncertainties on the fluxes and exploring the details of solar neutrino oscillations. This, together with the results from other future neutrino experiments such as Hyper-Kamiokande and DUNE, will provide new insight in some of the open issues of solar and neutrino physics, such as the metallicity problem and possible non standard interactions of neutrinos.

Acknowledgments

We are grateful for the ongoing cooperation from the China General Nuclear Power Group. This work was supported by the Chinese Academy of Sciences, the National Key R&D Program of China, the CAS Center for Excellence in Particle Physics, Wuyi University, and the Tsung-Dao Lee Institute of Shanghai Jiao Tong University in China, the Institut National de Physique Nucléaire et de Physique de Particules (IN2P3) in France, the Istituto Nazionale di Fisica Nucleare (INFN) in Italy, the Italian-Chinese collaborative research program MAECI-NSFC, the Fond de la Recherche Scientifique (F.R.S-FNRS) and FWO under the “Excellence of Science – EOS” in Belgium, the Conselho Nacional de Desenvolvimento Científico e Tecnológico in Brazil, the Agencia Nacional de Investigacion y Desarrollo and ANID - Millennium Science Initiative Program - ICN2019_044 in Chile, the Charles University Research Centre and the Ministry of Education, Youth, and Sports in Czech Republic, the Deutsche Forschungsgemeinschaft (DFG), the Helmholtz Association, and the Cluster of Excellence PRISMA+ in Germany, the Joint Institute of Nuclear Research (JINR) and Lomonosov Moscow State University in Russia, the joint Russian Science Foundation (RSF) and National Natural Science Foundation of China (NSFC) research program, the MOST and MOE in Taiwan, the Chulalongkorn University and Suranaree University of Technology in Thailand, University of California at Irvine and the National Science Foundation in USA.

References

- [1] N. Vinyoles, A.M. Serenelli, F.L. Villante, S. Basu, J. Bergström, M.C. Gonzalez-Garcia et al., *A New Generation of Standard Solar Models*, *Astrophys. J.* **835** (2017) .
- [2] I. Esteban, M.C. Gonzalez-Garcia, M. Maltoni, I. Martinez-Soler and T. Schwetz, *Updated fit to three neutrino mixing: exploring the accelerator-reactor complementarity*, *J. High Energ. Phys.* **01** (2017) 087.
- [3] BOREXINO collaboration, *Constraints on flavor-diagonal non-standard neutrino interactions from Borexino Phase-II*, *JHEP* **02** (2020) 038.
- [4] R. Davis, *Nobel lecture: A half-century with solar neutrinos*, *Rev. Mod. Phys.* **75** (2003) .
- [5] GALLEX collaboration, *Solar neutrinos observed by GALLEX at Gran Sasso*, *Nuclear Physics B - Proceedings Supplements* **31** (1993) 117.
- [6] GNO collaboration, *Complete results for five years of GNO solar neutrino observations*, *Physics Letters B* **616** (2005) 174.
- [7] SAGE collaboration, *Results from SAGE (The Russian-American gallium solar neutrino experiment)*, *Physics Letters B* **328** (1994) 234.
- [8] KAMIOKANDE collaboration, *Solar neutrino data covering solar cycle 22*, *Phys. Rev. Lett.* **77** (1996) 1683.
- [9] SUPER-KAMIOKANDE collaboration, *Measurements of the Solar Neutrino Flux from Super-Kamiokande's First 300 Days*, *Phys. Rev. Lett.* **81** (1998) 1158.
- [10] SNO collaboration, *Direct evidence for neutrino flavor transformation from neutral current interactions in the Sudbury Neutrino Observatory*, *Phys. Rev. Lett.* **89** (2002) 011301.
- [11] BOREXINO collaboration, *The Borexino detector at the Laboratori Nazionali del Gran Sasso*, *Nucl. Instrum. Meth. A* **600** (2009) 568.
- [12] BOREXINO collaboration, *Comprehensive measurement of pp-chain solar neutrinos*, *Nature* **562** (2018) 505.
- [13] BOREXINO collaboration, *Experimental evidence of neutrinos produced in the CNO fusion cycle in the Sun*, *Nature* **587** (2020) 577.
- [14] BOREXINO collaboration, *Improved Measurement of Solar Neutrinos from the Carbon-Nitrogen-Oxygen Cycle by Borexino and Its Implications for the Standard Solar Model*, *Phys.Rev.Lett.* **129** (2022) 252701.
- [15] BOREXINO collaboration, *First Directional Measurement of Sub-MeV Solar Neutrinos with Borexino*, *Phys. Rev. Lett.* **128** (2022) 091803.
- [16] BOREXINO collaboration, *Correlated and integrated directionality for sub-MeV solar neutrinos in Borexino*, *Phys. Rev. D* **105** (2022) 052002.
- [17] SNO collaboration, *Search for periodicities in the 8B solar neutrino flux measured by the Sudbury Neutrino Observatory*, *Phys. Rev. D* **72** (2005) 052010.
- [18] SUPER-KAMIOKANDE collaboration, *Solar neutrino measurements in Super-Kamiokande-I*, *Phys. Rev. D* **73** (2006) 112001.
- [19] BOREXINO collaboration, *Seasonal modulation of the 7Be solar neutrino rate in Borexino*, *Astropart. Phys.* **92** (2017) 21.
- [20] SUPER-KAMIOKANDE collaboration, *Precise measurement of the solar neutrino day-night and seasonal variation in Super-Kamiokande-I*, *Phys. Rev. D* **69** (2004) 011104.

- [21] SNO collaboration, *Electron energy spectra, fluxes, and day-night asymmetries of 8B solar neutrinos from measurements with NaCl dissolved in the heavy-water detector at the Sudbury Neutrino Observatory*, *Phys. Rev. C* **72** (2005) 055502.
- [22] BOREXINO collaboration, *Absence of day-night asymmetry of 862 keV 7Be solar neutrino rate in Borexino and MSW oscillation parameters*, *Phys. Lett. B* **707** (2012) 22.
- [23] E. Magg et al., *Observational constraints on the origin of the elements - IV. Standard composition of the Sun*, *Astron. Astrophys.* **661** (2022) A140.
- [24] G.D.O. Gann, K. Zuber, D. Bemmerer and A. Serenelli, *The Future of Solar Neutrinos*, *Ann. Rev. Nucl. Part. Sci.* **71** (2021) 491 [[2107.08613](#)].
- [25] JUNO collaboration, *Feasibility and physics potential of detecting 8B solar neutrinos at JUNO*, *Chinese Physics C* **45** (2021) 023004.
- [26] JUNO collaboration, *Model Independent Approach of the JUNO 8B Solar Neutrino Program*, [2210.08437](#).
- [27] JUNO collaboration, *JUNO physics and detector*, *Progress in Particle and Nuclear Physics* **123** (2022) 103927.
- [28] JUNO collaboration, *Sub-percent precision measurement of neutrino oscillation parameters with JUNO*, *Chin. Phys. C* **46** (2022) 123001.
- [29] JUNO collaboration, *Neutrino physics with JUNO*, *Journal of Physics G: Nuclear and Particle Physics* **43** (2016) 030401.
- [30] JUNO collaboration, *TAO Conceptual Design Report: A Precision Measurement of the Reactor Antineutrino Spectrum with Sub-percent Energy Resolution*, [2005.08745](#).
- [31] JUNO collaboration, *JUNO sensitivity to low energy atmospheric neutrino spectra*, *Eur. Phys. J. C* **81** (2021) 10.
- [32] R. Han, Y.-F. Li, L. Zhan, W.F. McDonough, J. Cao and L. Ludhova, *Potential of Geo-neutrino Measurements at JUNO*, *Chin. Phys. C* **40** (2016) 033003.
- [33] JUNO collaboration, *Prospects for detecting the diffuse supernova neutrino background with JUNO*, *JCAP* **10** (2022) 033.
- [34] H.-L. Li, Y.-F. Li, M. Wang, L.-J. Wen and S. Zhou, *Towards a complete reconstruction of supernova neutrino spectra in future large liquid-scintillator detectors*, *Phys. Rev. D* **97** (2018) 063014.
- [35] S. Wang, D.-M. Xia, X. Zhang, S. Zhou and Z. Chang, *Constraining primordial black holes as dark matter at JUNO*, *Phys. Rev. D* **103** (2021) 043010.
- [36] JUNO collaboration, *Optimization of the JUNO liquid scintillator composition using a Daya Bay antineutrino detector*, *Nucl. Instrum. Meth. A* **988** (2021) 164823.
- [37] JUNO collaboration, *The design and sensitivity of JUNO's scintillator radiopurity pre-detector OSIRIS*, *Eur. Phys. J. C* **81** (2021) .
- [38] OPERA collaboration, *The OPERA experiment target tracker*, *Nucl. Instrum. Meth. A* **577** (2007) 523.
- [39] JUNO collaboration, *Calibration Strategy of the JUNO Experiment*, *J. High Energ. Phys.* **03** (2021) 004 [[2011.06405](#)].
- [40] H.A. Bethe and C.L. Critchfield, *The formation of deuterons by proton combination*, *Phys. Rev.* **54** (1938) 248.
- [41] H.A. Bethe, *Energy production in stars*, *Phys. Rev.* **55** (1939) 434.
- [42] W. Fowler, *Experimental and theoretical nuclear astrophysics; the quest for the origin of the elements*, *Rev. Mod. Phys.* **56** (1984) .

- [43] S. Basu and H. Antia, *Helioseismology and solar abundances*, *Physics Reports* **457** (2008) 217.
- [44] E. Caffau, H.-G. Ludwig, M. Steffen, B. Freytag and P. Bonifacio, *Solar Chemical Abundances Determined with a CO5BOLD 3D Model Atmosphere*, *Solar Physics* **268** (2010) 255.
- [45] M. Asplund et al., *The Chemical Composition of the Sun*, *Annu. Rev. Astron. Astrophys.* **47** (2009) 481.
- [46] N. Grevesse and A. Sauval, *Standard Solar Composition*, *Space Science Reviews* **85** (1998) 161.
- [47] L. Wolfenstein, *Neutrino oscillations in matter*, *Phys. Rev. D* **17** (1978) 2369.
- [48] S.P. Mikheyev and A.Y. Smirnov, *Resonance Amplification of Oscillations in Matter and Spectroscopy of Solar Neutrinos*, *Sov. J. Nucl. Phys.* **42** (1985) 913.
- [49] P. de Holanda, W. Liao and A. Smirnov, *Toward precision measurements in solar neutrinos*, *Nuclear Physics B* **702** (2004) 307–332.
- [50] JUNO collaboration, *Radioactivity control strategy for the JUNO detector*, *J. High Energ. Phys.* **11** (2021) .
- [51] BOREXINO collaboration, *Simultaneous Precision Spectroscopy of pp, ^7Be , and pep Solar Neutrinos with Borexino Phase-II*, *Phys. Rev. D* **100** (2019) 082004.
- [52] BOREXINO collaboration, *Final results of Borexino Phase-I on low energy solar neutrino spectroscopy*, *Phys. Rev. D* **89** (2014) 112007.
- [53] KamLAND collaboration, *^7Be Solar Neutrino Measurement with KamLAND*, *Phys. Rev. C* **92** (2015) 055808.
- [54] BOREXINO collaboration, *Neutrinos from the primary proton–proton fusion process in the Sun*, *Nature* **512** (2014) 384.
- [55] KamLAND collaboration, *Production of radioactive isotopes through cosmic muon spallation in KamLAND*, *Phys. Rev. C* **81** (2010) 025807.
- [56] M. Ambrosio et al., *Measurement of the residual energy of muons in the Gran Sasso underground laboratories*, *Astropart. Phys.* **19** (2003) 313.
- [57] BOREXINO collaboration, *Cosmogenic Backgrounds in Borexino at 3800 m water-equivalent depth*, *Journal of Cosmology and Astropart. Phys.* **2013** (2013) 049.
- [58] BOREXINO collaboration, *Identification of the cosmogenic ^{11}C background in large volumes of liquid scintillators with Borexino*, *Eur. Phys. J. C* **81** (2021) .
- [59] V.I. Kopeikin, *Flux and Spectrum of Reactor Antineutrinos*, *Physics of Atomic Nuclei* **75** (2012) 143–152.
- [60] X.B. Ma, W.L. Zhong, L.Z. Wang, Y.X. Chen and J. Cao, *Improved calculation of the energy release in neutron-induced fission*, *Phys. Rev. C* **88** (2012) .
- [61] T. Lin et al., *Simulation Software of the JUNO Experiment*, [2212.10741](#).
- [62] A. Savitzky and M.J.E. Golay, *Smoothing and differentiation of data by simplified least squares procedures*, *Analytical Chemistry* **36** (1964) 1627.
- [63] F. Vissani, *Luminosity constraint and entangled solar neutrino signals*, in *5th International Solar Neutrino Conference*, pp. 121–141, 2019.
- [64] J. Bergstrom, M.C. Gonzalez-Garcia, M. Maltoni, C. Pena-Garay, A. Serenelli and N. Song, *Updated determination of the solar neutrino fluxes from solar neutrino data*, *J. High Energ. Phys.* **03** (2016) 132.
- [65] F. Capozzi, E. Lisi, A. Marrone and A. Palazzo, *Current unknowns in the three neutrino framework*, *Prog. Part. Nucl. Phys.* **102** (2018) 48.

- [66] BOREXINO collaboration, *Independent determination of the Earth's orbital parameters with solar neutrinos in Borexino*, *Astropart. Phys.* **92** (2022) 102778.
- [67] E.K. Akhmedov, M.A. Tortola and J.W.F. Valle, *A simple analytic three-flavour description of the day-night effect in the solar neutrino flux*, *J. High Energ. Phys.* **2004** (2004) 057.
- [68] J.N. Bahcall, M.C. Gonzalez-Garcia and C. Pena-Garay, *Robust signatures of solar neutrino oscillation solutions*, *J. High Energ. Phys.* **04** (2002) 007.
- [69] R. Plestid, *Luminous solar neutrinos. I. Dipole portals*, *Phys. Rev. D* **104** (2021) 075027.
- [70] R. Plestid, *Luminous solar neutrinos. II. Mass-mixing portals*, *Phys. Rev. D* **104** (2021) 075028.
- [71] V. Brdar, J. Kopp, J. Liu, P. Prass and X. Wang, *Fuzzy dark matter and nonstandard neutrino interactions*, *Phys. Rev. D* **97** (2018) 043001.
- [72] V. Brdar, A. Greljo, J. Kopp and T. Opferkuch, *The Neutrino Magnetic Moment Portal*, in *55th Rencontres de Moriond on Electroweak Interactions and Unified Theories*, 5, 2021.
- [73] J.N. Bahcall and A. Ulmer, *Temperature dependence of solar neutrino fluxes*, *Phys. Rev. D* **53** (1996) 4202.
- [74] J.N. Bahcall and P. Kumar, *G-Modes and the Solar Neutrino Problem*, *Astrophys. J. Lett.* **409** (1993) L73.
- [75] SNO collaboration, *Searches for high-frequency variations in the 8B solar neutrino flux at the Sudbury Neutrino Observatory*, *Astrophys. J.* **710** (2010) 540.
- [76] Lopes, I. and Turck-Chièze, S., *Detecting Gravity Modes in the Solar 8 B Neutrino Flux*, *Astrophys. J.* **792** (2014) .
- [77] N.R. Lomb, *Least-squares frequency analysis of unequally spaced data*, *Astrophysics and space science* **39** (1976) 447.
- [78] J. Scargle, *Studies in astronomical time series analysis. ii - statistical aspects of spectral analysis of unevenly spaced data*, *Astrophys. J.* **263** (1983) .
- [79] SUPER-KAMIOKANDE collaboration, *Search for periodic modulations of the solar neutrino flux in Super-Kamiokande-I*, *Phys. Rev. D* **68** (2003) 092002.